



LIDAR Wind Speed Measurement Analysis and Feed-Forward Blade Pitch Control for Load Mitigation in Wind Turbines

January 2010 — January 2011

F. Dunne, E. Simley, and L.Y. Pao
*University of Colorado
Boulder, Colorado*

NREL is a national laboratory of the U.S. Department of Energy, Office of Energy Efficiency & Renewable Energy, operated by the Alliance for Sustainable Energy, LLC.

Subcontract Report
NREL/SR-5000-52098
October 2011

Contract No. DE-AC36-08GO28308

This publication received minimal editorial review at NREL.

NOTICE

This report was prepared as an account of work sponsored by an agency of the United States government. Neither the United States government nor any agency thereof, nor any of their employees, makes any warranty, express or implied, or assumes any legal liability or responsibility for the accuracy, completeness, or usefulness of any information, apparatus, product, or process disclosed, or represents that its use would not infringe privately owned rights. Reference herein to any specific commercial product, process, or service by trade name, trademark, manufacturer, or otherwise does not necessarily constitute or imply its endorsement, recommendation, or favoring by the United States government or any agency thereof. The views and opinions of authors expressed herein do not necessarily state or reflect those of the United States government or any agency thereof.

Available electronically at <http://www.osti.gov/bridge>

Available for a processing fee to U.S. Department of Energy and its contractors, in paper, from:

U.S. Department of Energy
Office of Scientific and Technical Information

P.O. Box 62
Oak Ridge, TN 37831-0062
phone: 865.576.8401
fax: 865.576.5728
email: <mailto:reports@adonis.osti.gov>

Available for sale to the public, in paper, from:

U.S. Department of Commerce
National Technical Information Service
5285 Port Royal Road
Springfield, VA 22161
phone: 800.553.6847
fax: 703.605.6900
email: orders@ntis.fedworld.gov
online ordering: <http://www.ntis.gov/help/ordermethods.aspx>

Cover Photos: (left to right) PIX 16416, PIX 17423, PIX 16560, PIX 17613, PIX 17436, PIX 17721



Printed on paper containing at least 50% wastepaper, including 10% post consumer waste.

LIDAR Wind Speed Measurement Analysis and Feed-Forward Blade Pitch Control for Load Mitigation in Wind Turbines

January 2010 — January 2011

F. Dunne, E. Simley, and L.Y. Pao
*University of Colorado
Boulder, Colorado*

NREL Technical Monitor: Alan D. Wright
Prepared under Subcontract No(s). XEE-9-99404-01

NREL is a national laboratory of the U.S. Department of Energy, Office of Energy Efficiency & Renewable Energy, operated by the Alliance for Sustainable Energy, LLC.

Abstract

Light Detection and Ranging (LIDAR) systems are able to measure the speed of incoming wind before it interacts with a wind turbine rotor. These preview wind measurements can be used in feed-forward control systems designed to reduce turbine loads. However, the degree to which such preview-based control techniques can reduce loads by reacting to turbulence depends on how accurately the incoming wind field can be measured. The first half of this report examines the accuracy of different measurement scenarios that rely on coherent continuous-wave or pulsed Doppler LIDAR systems to determine their applicability to feed-forward control. In particular, the impacts of measurement range and angular offset from the wind direction are studied for various wind conditions. A realistic case involving a scanning LIDAR unit mounted in the spinner of a wind turbine is studied in depth with emphasis on choices for scan radius and preview distance. The effects of turbulence parameters on measurement accuracy are studied as well. Continuous-wave and pulsed LIDAR models based on typical commercially available units were used in the studies present in this report.

The second half of this report discusses feed-forward control system designs that use preview wind measurements. Combined feedback/feed-forward blade pitch control is compared to industry standard feedback control when simulated in realistic turbulent above-rated winds. The feed-forward controllers are designed to reduce fatigue loads, increasing turbine lifetime and therefore reducing the cost of energy. Three feed-forward designs are studied: non-causal series expansion, Preview Control, and optimized FIR filter. The input to the feed-forward controller is a measurement of incoming wind speeds that could be provided by LIDAR. Non-causal series expansion and Preview Control methods reduce blade root loads but increase tower bending in simulation results. The optimized FIR filter reduces loads overall, keeps pitch rates low, and maintains rotor speed regulation and power capture, while using imperfect wind measurements provided by the spinning continuous-wave LIDAR model.

List of Acronyms, Abbreviations, and Nomenclature

b	Collective blade pitch feed-forward command
d	Measurement preview distance
Δp	Length of range gate for a pulsed LIDAR
Δr	Full-width-at-half-maximum pulse width
F	Focal distance or feed-forward controller
k	Wind velocity wave number (m^{-1})
o	Output error
P	Linearized model of wind turbine
r	Scan radius for spinning LIDAR
R	Distance to center of range gate for a pulsed LIDAR
σ_u	Standard deviation of u component of wind velocity
θ	LIDAR measurement angle
\bar{u}	Mean u wind speed
u^*	Friction velocity
U_D^*	Average friction velocity over rotor disk
φ	Angle between laser and wind velocity vector
ψ	Angle in rotor plane
ω	Rotational rate of spinning LIDAR (RPM)
AR	Above rated wind speed
bcmd	Collective blade pitch error
CP	Collective pitch
CW	Continuous wave
DEL	Damage equivalent load
DOF	Degree of freedom
FAST	Aeroelastic wind turbine simulator
IP	Individual pitch
LIDAR	Light detection and ranging
LLJ	Low level jet
MBC	Multi-blade coordinate
$P_{ob_{cmd}}$	Open-loop turbine transfer function from collective pitch error to output error
P_{ow}	Open-loop turbine transfer function from wind speed error to output error
PI	Proportional-integral
RMS	Root mean square
TI	Turbulence intensity
T_{ob}	Closed-loop transfer function from collective pitch feed-forward command to output error
T_{ow}	Closed-loop transfer function from wind speed error to output error

Table of Contents

1	LIDAR Modeling Introduction.....	7
2	LIDAR Measurement Theory.....	8
2.1	Continuous Wave Range Weighting.....	10
2.2	Measurement Geometry.....	12
2.3	Combined Range Weighting and Geometrical Errors.....	13
2.4	Pulsed LIDAR Systems.....	15
3	LIDAR Simulation Results.....	17
3.1	Wind Conditions.....	18
3.2	Impact of Turbulence on Measurement Errors.....	19
3.3	Hub Mounted Spinning LIDAR Analysis.....	22
4	LIDAR Modeling Conclusions and Future Work.....	27
5	Feed-Forward Control Introduction.....	30
6	Simulated Turbine and Turbulent Inflow.....	31
6.1	5 MW Turbine Model and Baseline Control.....	31
6.2	Wind Fields.....	32
7	Non-Causal Series Expansion.....	32
7.1	Design.....	32
7.2	Results.....	35
8	Preview Control.....	36
8.1	Design.....	36
8.2	Results.....	38
9	Optimized FIR Filter.....	43
9.1	Design.....	43
9.1.1	Cost Function.....	45
9.1.2	Constraints.....	45
9.1.3	Seeds.....	45
9.1.4	Creation Function.....	46
9.2	Results.....	46
10	Feed-Forward Control Conclusions.....	49
11	Overall Conclusions and Future Work.....	49
12	References.....	50

List of Figures

Figure 1. Block Diagram illustrating how LIDAR can be used in a combined feedforward/feedback control scenario.....	7
Figure 2. Coordinate system and measurement variables for LIDAR analysis.....	9
Figure 3. Range weighting functions.....	11
Figure 4. Frequency response of range weighting functions.....	11
Figure 5. The effects of measurement angle and range on measurement error.....	14
Figure 6. Illustration of range weighting and measurement angle errors.....	15
Figure 7. Comparison of CW and pulsed LIDARs.....	17
Figure 8. CW measurement error vs. turbulence intensity.....	20
Figure 9. CW measurement error vs. local friction velocity.....	21
Figure 10. Pulsed and CW Measurement errors vs. local friction velocity.....	22
Figure 11. Measurement error vs. preview distance for various scan radii.....	23
Figure 12. Minimum achievable errors and optimal preview distances vs. scan radius.....	24
Figure 13. Friction velocity profiles.....	25
Figure 14. Minimum achievable errors and optimal preview distances for all wind conditions..	26
Figure 15. Measurement error vs. preview distance for CW and pulsed LIDARs.....	27
Figure 16. Measurement error example with a coherent structure.....	29
Figure 17. Feedback Only Control.....	30
Figure 18. Combined Feedback/Feedforward Control.....	31
Figure 19. Linear plant model.....	32
Figure 20. Combined Feedback/Feedforward Control.....	33
Figure 21. Non-Causal Series Expansion (NCSE) feedforward control.....	35
Figure 22. A comparison of Damage Equivalent Loads (DELs) and nacelle RMS velocities, NCSE.....	36
Figure 23. Preview Control pulse response for varying preview lengths.....	38
Figure 24. Linear turbine model response comparing Preview Control to no Preview Control..	39
Figure 25. Bode magnitude plot of linear turbine model with Preview Control.....	40
Figure 26. Simulated nonlinear turbine model with Preview Control, step response.....	41
Figure 27. Simulated nonlinear turbine model with Preview Control, sine response.....	42
Figure 28. Time series comparing baseline collective pitch feedback control with and without Preview Control in wind field AR2_s1.....	42
Figure 29. A comparison of Damage Equivalent Loads (DELs) and nacelle RMS velocities, Preview Control.....	43
Figure 30. Pulse responses.....	44
Figure 31. Impulse response of the Optimized FIR filter.....	46
Figure 32. Bode magnitude plot of the Optimized FIR filter.....	47
Figure 33. Damage equivalent loads, RMS nacelle accelerations, and RMS pitch rate of IP Baseline control without and with Optimized FIR feedforward, AR1-3.....	48
Figure 34. Damage equivalent loads, RMS nacelle accelerations, and RMS pitch rate of IP Baseline control without and with Optimized FIR feedforward, AR4-5.....	48

List of Tables

Table 1. A Summary of the Great Plains Low Level Jet Wind Fields Used for Wind Speed Measurement Analysis.	18
---	----

1 LIDAR Modeling Introduction

Wind speed measurements in front of a wind turbine can be used as part of feed-forward or preview-based controllers to help mitigate structural loads caused by turbulent wind conditions. Prior analyses have shown that improvements to turbine load performance can be achieved with knowledge of the incoming wind field [1,2,3]. A block diagram of such a control strategy is shown in Figure 1. Upstream wind is measured, providing an estimate of the wind speeds that will eventually reach the turbine. In reality, the turbulent structures in the wind will evolve between the time they are measured and when they reach the turbine, causing errors in the preview wind measurements [4]. This report focuses on the preview measurement stage, ignoring wind evolution. Thus, the authors' model assumes the validity of Taylor's frozen turbulence hypothesis, which states that turbulent eddies tend to remain unchanged while advecting with the average wind velocity [5].

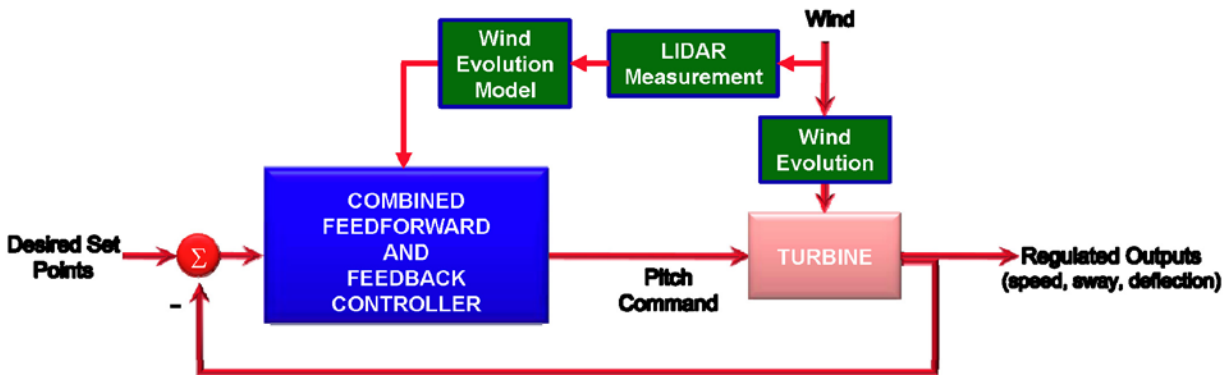


Figure 1. A block diagram illustrating how LIDAR can be used in a preview based combined feed-forward/feedback control scenario. Although wind measured using LIDAR will evolve between preview measurement and contact with the turbine, wind evolution is not studied in this report.

Although various optical and acoustical methods exist for measuring wind speeds, coherent Doppler LIDAR (light detection and ranging) provides the most accurate and versatile way to provide remote measurements [6]. The two main coherent LIDAR technologies that are currently available are continuous wave (CW) LIDAR and pulsed LIDAR. In this report, we provide an analysis of using both CW and pulsed LIDAR technologies to provide preview wind measurements, with an emphasis on CW. Aside from the technological merits of CW LIDAR, the recent application of fiber telecommunications technology to LIDAR instrumentation has made infrared, CW LIDAR an economical and eye-safe technology for measuring wind velocity in front of a turbine [6].

While some improvement can be gained by measuring wind speeds upwind of the hub location, it is much more advantageous to be able to measure the wind that will appear at each individual blade [7]. A commercially available CW LIDAR mounted in the spinner of a wind turbine has been successfully tested in the field, illustrating the ability of the technology to be applied to individual turbine control [8]. Therefore, we provide a detailed analysis of preview wind measurements at a variety of blade span positions using a spinning LIDAR mounted in the hub of a 5 MW turbine. Analyses are provided using separate CW and pulsed LIDAR models

developed for the National Renewable Energy Laboratory's (NREL's) FAST (Fatigue, Aerodynamics, Structures, and Turbulence) code [9]. The CW and pulsed models are based on commercially available LIDARs. The LIDAR measurement scenarios investigated involve NREL's reference 5 MW model [10] with turbulent wind inputs generated using NREL's TurbSim code [11,12].

The LIDAR modeling section of the report is organized as follows. Section 2 presents the principal equation used in the LIDAR measurement models, called the “range weighting function,” as well as the geometry of LIDAR measurements. The processes through which range weighting and measurement geometry cause measurement errors are discussed here. A subsection is then devoted to explaining the differences between CW and pulsed LIDARs and a derivation of the pulsed LIDAR range weighting function is provided. Section 3 describes the results from a simulation of the effects of wind turbulence parameters on wind speed measurement error. Section 3 also describes the investigation of a hub-mounted spinning LIDAR scenario, with a focus on the optimal preview distances for wind speed measurements at given fractions of the rotor radius. Section 4 concludes the LIDAR modeling portion of the report and provides a discussion of plans for future research involving LIDAR and wind evolution modeling.

2 LIDAR Measurement Theory

The analysis of LIDAR performance examined here uses the coordinate system shown in Figure 2 (a). The ground referenced x , y , and z axes are defined such that $-z$ is pointing in the direction of gravity and x is nominally pointing in the downwind direction. However, depending on the wind conditions being simulated, the x axis may not be aligned with the average wind direction. The wind speed vector is defined by u , v , and w components, where u is the streamwise component. Nominally, the u , v , and w axes are aligned with the x , y , and z axes, respectively, since the FAST simulations simply “march” the wind toward the turbine in the x direction. The 5 MW model used for these LIDAR studies has a hub height of 90 meters and a rotor radius of 63 meters.

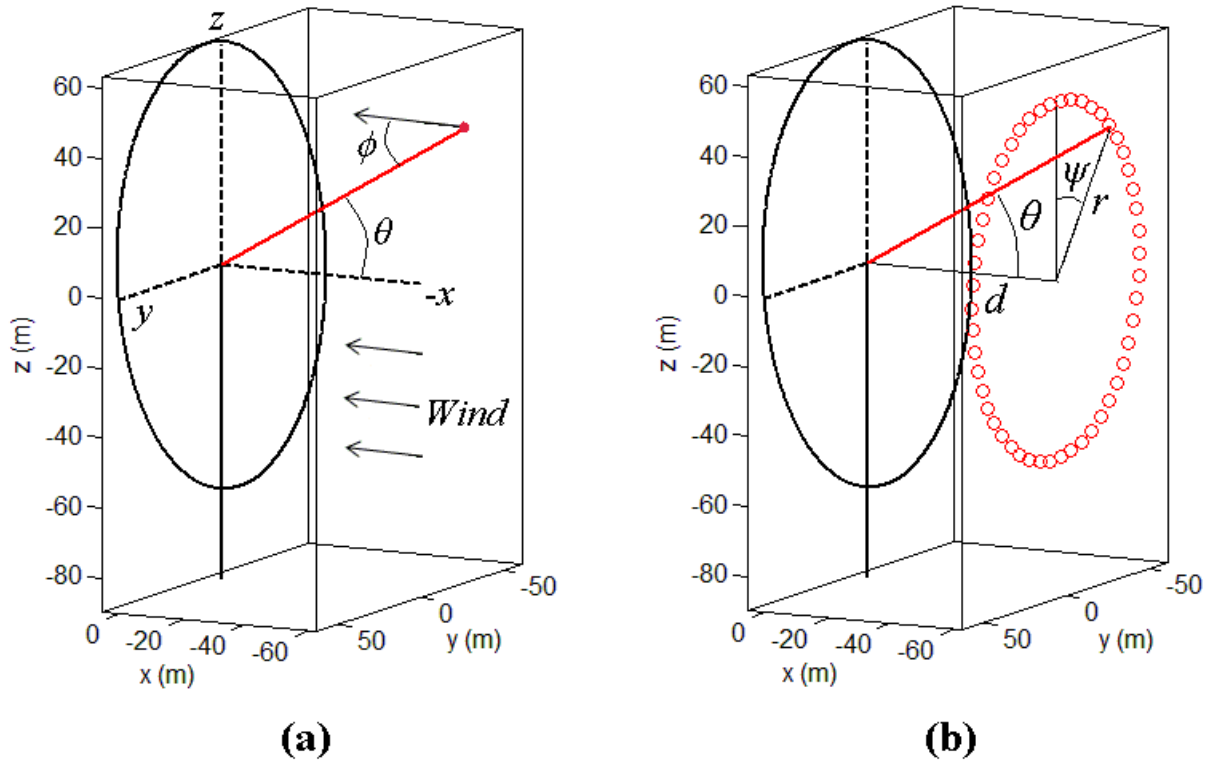


Figure 2. Coordinate system and measurement variables referred to in the discussions. (a) The x , y , z coordinate system along with the LIDAR measurement angle, θ , and the angle between the LIDAR beam and the wind speed vector, ϕ . (b) Variables referred to in the analysis of a spinning LIDAR including preview distance, d , and scan radius, r .

The LIDAR measurement model introduces two imperfections to wind speed measurements. Range weighting is the effect inherent to CW and pulsed LIDAR that applies a spatial filter along the laser beam, causing wind speeds at locations other than the focal distance to contribute to the measured value. The other primary source of error in wind speed measurements is due to estimating the u component of the wind velocity vector given a single line-of-sight measurement. This is sometimes called the “cyclops dilemma.” Control systems utilizing preview wind speed measurements primarily focus on the component of the wind that is perpendicular to the rotor plane, nominally the u component. In our simulations, the mean streamwise wind direction is aligned with the x axis, so we are assuming that the rotor plane is always perpendicular to the x axis. Therefore, our LIDAR measurements estimate the component of wind aligned with the x axis, which will be treated as equivalent to the u component for the rest of the report. When the LIDAR is pointing in the x direction, there will be no geometrical measurement errors because the v and w components do not contribute to the detected radial velocity. If the laser is instead pointed in a direction other than along the x axis, unknown v and w components contribute to the measurement and an estimate of the u component must be formed.

The errors due to measurement geometry are equivalent for CW and pulsed technologies, but effects due to range weighting are different. Whereas the range weighting function for CW LIDAR changes for every measurement range, it remains constant for all ranges with a pulsed

LIDAR. Therefore there are fewer variables to consider when analyzing pulsed LIDAR and the emphasis of this report is on CW LIDAR.

2.1 Continuous Wave Range Weighting

CW LIDAR determines the radial wind speed at a specific location by focusing the laser beam at that location instead of relying on range gates and timing circuitry like a pulsed system. However, rather than only detecting the wind speed at the focal point, wind speed values along the entire laser beam are integrated according to a range weighting function $W(R)$, inherent in the physics of a focused LIDAR system, to yield the detected value. Our model assumes that range weighting occurs only along an infinitely thin beam. The wind speed measurement due to range weighting at a focal distance F is determined by

$$v_{wgt}(F) = \int_{-\infty}^{\infty} v_r(R)W(R)dR \quad (2.1)$$

where $v_r(R)$ is the radial velocity at a range R along the laser beam [13]. In the case when the effects of refractive turbulence on laser propagation are ignored, the range weighting function for a focal distance of F is given by

$$W(R) = \frac{K_N}{R^2 + \left(1 - \frac{R}{F}\right)^2 R_R^2} \quad (2.2)$$

where R_R is the Rayleigh range and K_N is a normalizing constant so that

$$\int_{-\infty}^{\infty} W(R)dR = 1. \quad (2.3)$$

The Rayleigh range is given by

$$R_R = \frac{\pi a_2^2}{\lambda} \quad (2.4)$$

where λ is the laser wavelength and a_2 is the e^{-2} intensity radius of the Gaussian laser beam. The analyses in this study assume $\lambda = 1.565 \mu\text{m}$ and $a_2 = 2.8 \text{ cm}$, which are characteristic of a commercially available CW Doppler LIDAR system.

$W(R)$ is presented in Figure 3 for several ranges that might be desired in wind preview control applications. Clearly, as the range of the measurement increases, the detected velocity contains increasingly significant contributions from a greater length along the beam. The spatial averaging effect of range weighting causes the LIDAR beam to low-pass filter the wind speeds it measures. As focal distance increases, the cut-off frequency of the equivalent filter decreases. Frequency responses for the range weighting functions shown in Figure 3 as well as those for focal distances of 200 and 250 meters are provided in Figure 4. In addition, Figure 4 shows the range weighting function for a commercially available pulsed LIDAR discussed in Section 2.4 and a typical wind spectrum used in this research. Note that typical focal distances for a CW LIDAR are less than 200 meters.

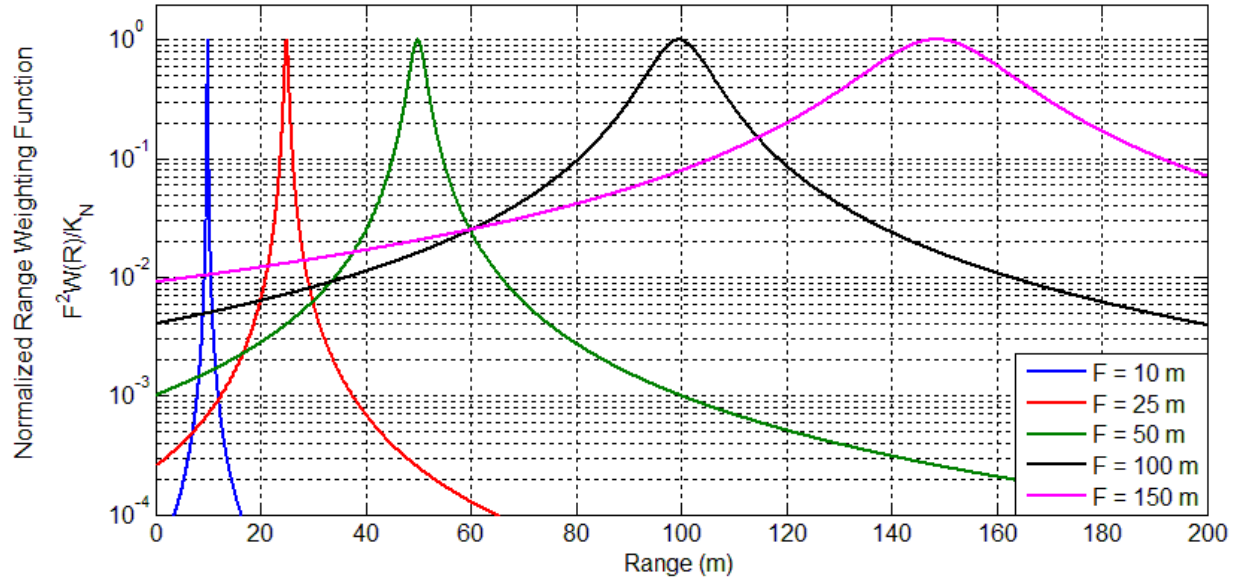


Figure 3. Normalized range weighting functions, $W(R)$, for the CW LIDAR at a variety of focal distances, F . The range weighting functions spatially average the wind along the laser beam. As focal distance increases, spatial averaging along a greater length of the beam occurs.

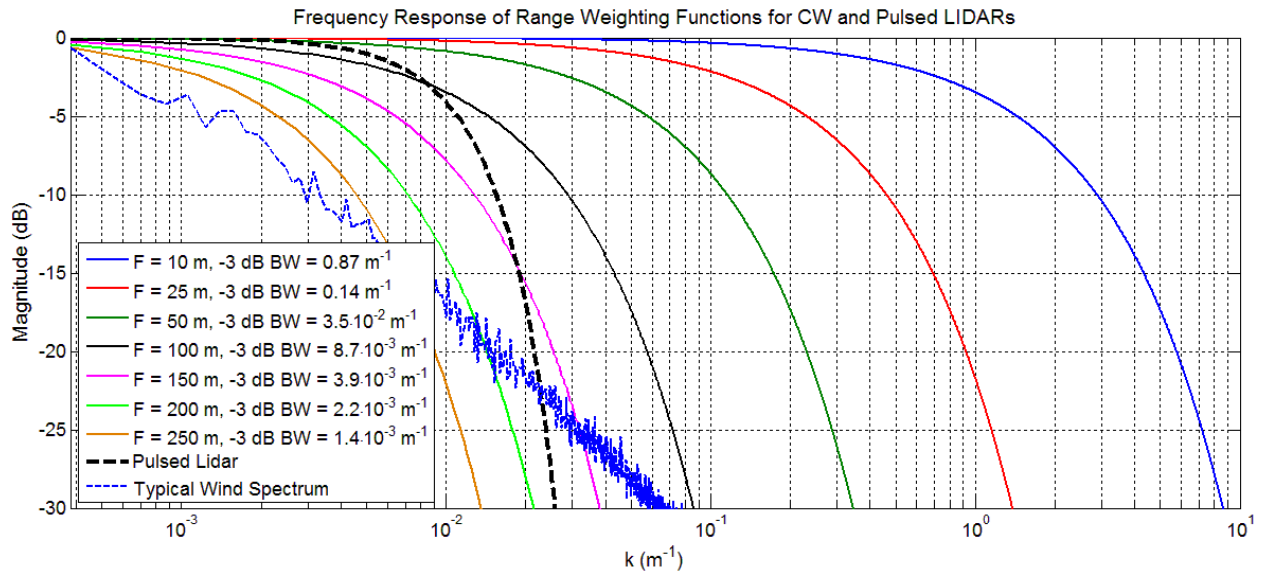


Figure 4. The frequency responses of the normalized range weighting filters for a variety of focal distances along with the -3 dB bandwidths of the filters.

The -3 dB bandwidths of the CW LIDAR range weighting functions listed in Figure 4 are inversely related to the square of the focal distance through a simple formula based on observations. The -3 dB bandwidth is given by

$$BW = \frac{87}{F^2} \quad (2.5)$$

where the factor of 87 is based on the specific LIDAR parameters used in this report.

Figure 4 can be used to determine the frequency responses of measurement error for various focal distances. The range weighting filters affect the magnitude of the measured wind but do not introduce any phase distortion. An implication of this is that the magnitude of measured wind as a function of spatial frequency is reduced by a factor of

$$err(k) = (1 - |W(k)|) \quad (2.6)$$

where $W(k)$ is the frequency response of the range weighting function, while the phase is unchanged. Using Eq. 2.6, the RMS measurement error as a function of frequency is found to be

$$\sigma_{err}(k) = \frac{(1 - |W(k)|)|U(k)|}{\sqrt{2}} \quad (2.7)$$

where $U(k)$ is the frequency response of the u component of the wind.

2.2 Measurement Geometry

A single LIDAR unit is capable of measuring only radial wind velocity, yet the wind velocity at a given location is a vector quantity consisting of u , v , and w components. Therefore, a single LIDAR cannot determine the entire wind vector quantity. Instead, the assumption that the measured radial wind speed is due to the u component alone with $v = w = 0$ is made, since ideally $u \gg v, w$. When the LIDAR is pointing upwind at an angle θ off of the x axis, it is assumed that the angle ϕ , which is formed between the instantaneous wind vector and LIDAR beam, is equal to θ (although ϕ and θ will differ if the instantaneous wind direction is not aligned with the x axis, as is almost always the case). The detected radial velocity (see Figure 2) is then given by

$$v_r = \sqrt{u^2 + v^2 + w^2} \cos(\phi) \quad (2.8)$$

and under the assumption that $v = w = 0$ ($\phi = \theta$), the estimate of u is

$$\hat{u} = \frac{v_r}{\cos(\theta)}. \quad (2.9)$$

When the LIDAR is pointing nearly along the x axis, and θ is small, errors due to the LIDAR geometry will be small since the measured radial velocity will be dominated by the u component of wind speed. As θ increases, the radial velocity measured by the LIDAR will contain more contributions from the v and w components. For large angles off of the x axis where the u component becomes close to orthogonal to the LIDAR direction, θ is close to $\pi/2$ and an approximation of the u estimate is

$$\hat{u} \approx \sqrt{u^2 + v^2 + w^2} \frac{\pi/2 - \phi}{\pi/2 - \theta}. \quad (2.10)$$

For large θ and ϕ , close to $\pi/2$, the u estimate is very sensitive to mismatches between θ and ϕ and measurements will likely contain severe errors.

An analysis of large angle errors has shown that for a variable u velocity, and a transverse wind speed component with fixed magnitude $\alpha = \sqrt{v^2 + w^2}$ and uniformly distributed random direction in the yz plane, the RMS measurement error will be

$$\sigma_{err} = \frac{\alpha \tan \theta}{\sqrt{2}} \quad (2.11)$$

where θ is the measurement angle off of the x axis. Furthermore, for stochastic wind fields where the magnitude $\sqrt{v^2 + w^2}$ varies with time, the RMS error is given by

$$\sigma_{err} = \frac{\alpha_{RMS} \tan \theta}{\sqrt{2}} \quad (2.12)$$

where α_{RMS} is the RMS value of the transverse wind speed magnitude, or $\sqrt{v^2 + w^2}$. The most revealing feature of this relationship is that in the absence of range weighting, measurement errors will scale with $\tan \theta$.

2.3 Combined Range Weighting and Geometrical Errors

An analysis has been provided for range weighting errors and measurement angle errors separately, but in practice measurement errors are caused by a combination of the two sources. For very large θ , angular errors tend to dominate, while for moderate to small θ and large focal distances, range weighting dominates the overall error. Figure 5 (a) illustrates how measurement errors follow a $\tan \theta$ trend for large θ as well as how range weighting will dominate overall CW measurement errors for small θ and great enough focal distances. The scenario used to generate the four curves in Figure 5 (a) is illustrated in Figure 5 (b). Each LIDAR is pointed at a different elevation, ΔZ , above the LIDAR unit, that does not vary with measurement angle. At any given

measurement angle, the focal distance is then given by $F = \frac{\Delta Z}{\sin \theta}$. Thus the curves representing large ΔZ have greater focal distances, and represent errors that are dominated by range weighting, at larger θ . Note that the chosen ΔZ represent 25%, 50%, 75%, and 100% blade span for the 5 MW turbine model investigated in this research. For larger θ (which correspond to smaller F for a constant ΔZ), measurement error follows the $\tan \theta$ curve. Each solid curve in (a) begins a transition (at a different measurement angle) from predominantly representing angular errors to being dominated by range weighting errors. The $\Delta Z = 63$ m curve diverges from $\tan \theta$ at roughly 40° and $F = 98$ meters, the $\Delta Z = 47.25$ m curve diverges at 33° and $F = 86$ meters, the $\Delta Z = 31.5$ m curve diverges at 27° and $F = 69$ meters, and the $\Delta Z = 15.75$ m curve diverges at 20° and $F = 46$ meters.

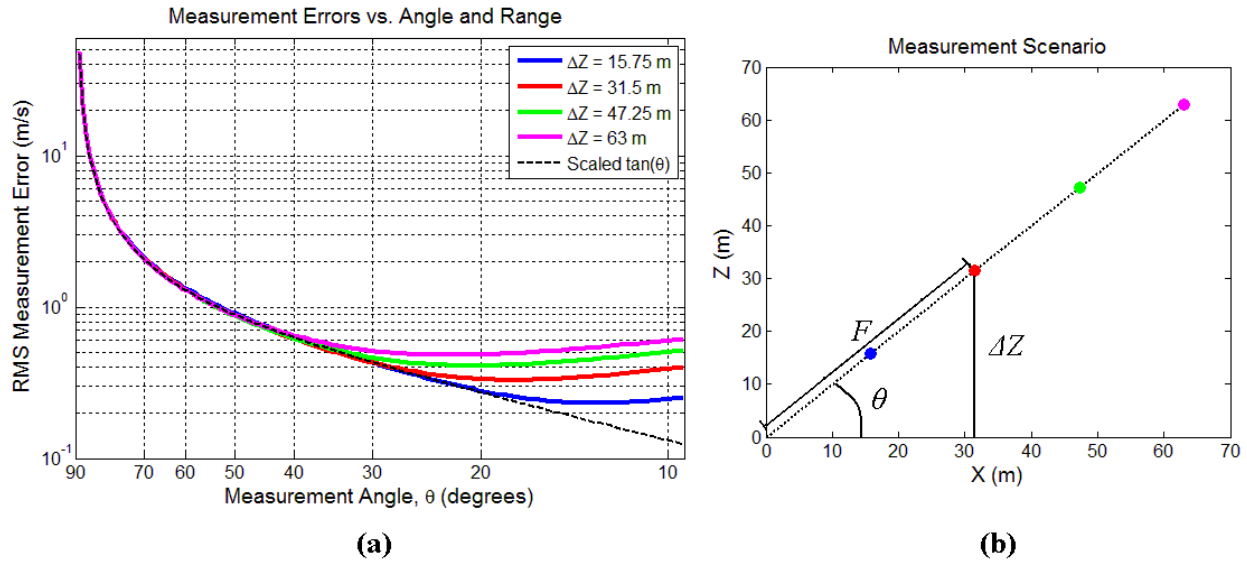


Figure 5. The combined effects of measurement angle and range weighting on overall measurement error for CW LIDAR. (a) Four curves showing RMS measurement error vs. measurement angle. The curves represent LIDAR measurements at four different fixed ΔZ values as a function of measurement angle θ . For each ΔZ , the focal distance F varies with measurement angle. The four different measurement scenarios are illustrated in (b).

To graphically illustrate how range weighting and measurement angles affect CW wind speed measurements, Figure 6 compares actual u components of wind speed as well as the measured wind speeds for a variety of F and θ . For $F = 10$ and $F = 25$ meters, range weighting has little impact on detected wind while for larger F , the low-pass filtering effect of the measurement process can clearly be observed in Figure 6 (a). Figure 6 (b) illustrates the severity of wind speed errors for moderate to large θ .

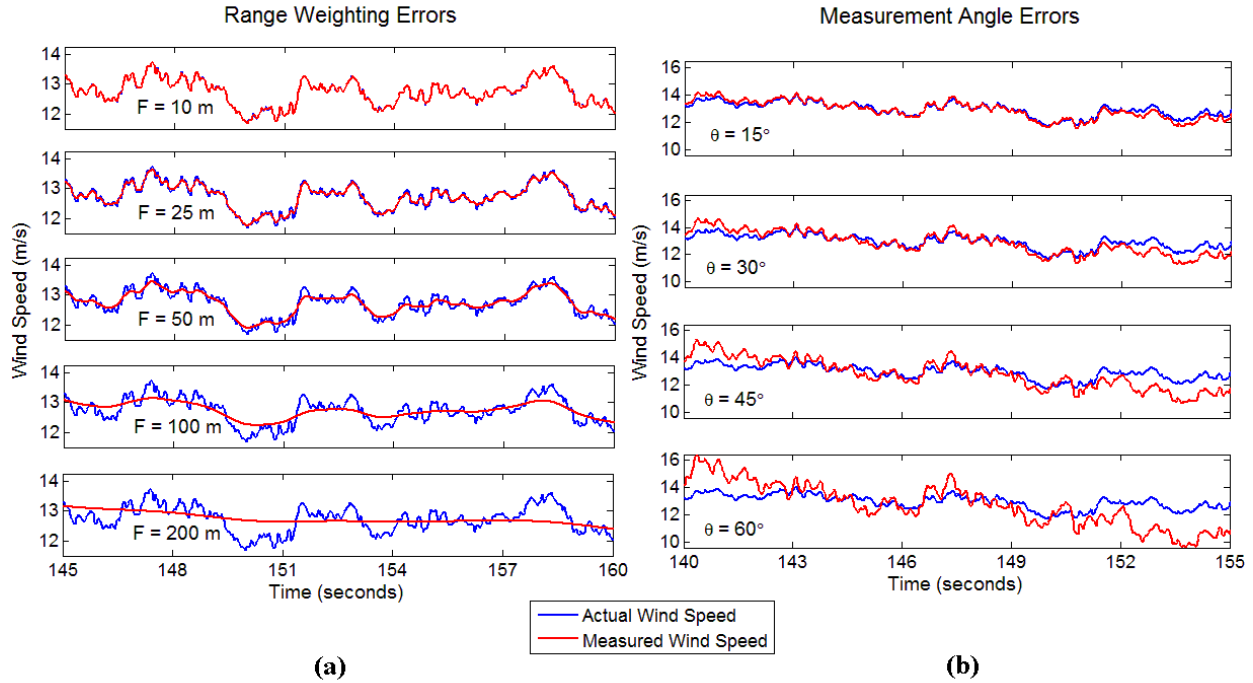


Figure 6. Examples of (a) range weighting errors for a variety of F and (b) measurement angle errors for a variety of θ . The measurements in (b) involve focal distances less than 10 m, so all visible discrepancies from the true wind speed are solely due to geometrical errors.

For the analysis of a spinning LIDAR described in Section 3.3, another possible source of measurement error exists. The CW LIDAR being modeled provides a velocity sample at a rate of 50 Hz. For a LIDAR that is pointed at some angle θ and spinning around the x axis, the focal point will travel along the circle being scanned while returns are being integrated to form a velocity estimate. This “blurring” effect could cause another source of spatial averaging error. The arc length that the focal point traverses during a sample period is equal to

$$l = \frac{2\pi r\omega}{50} \quad (2.13)$$

where ω is the rotational rate of the LIDAR and r is the scan radius as defined in Figure 2 (b). An investigation of this source of error showed that the blurring effect causes insignificant error for ω less than 240 RPM. Since it is unlikely that a spinning LIDAR would scan at a rate higher than 240 RPM, we have ignored this source of error. It is possible that the resolution of the wind files used during simulation is not high enough to reveal the severity of the spatial averaging that would occur. Investigating the effect with higher resolution wind fields is an area of future work.

2.4 Pulsed LIDAR Systems

Although pulsed LIDAR systems do not rely on focusing a laser at the range of interest as CW systems do, their spatial averaging can be similarly described by a range weighting function. Pulsed LIDARs emit a laser pulse and integrate the back-scattered light as the pulse travels through several "range gates." One drawback to using pulsed technology is that more time is required to integrate enough photons to provide a useful velocity estimate. The pulsed LIDAR

that the model is based on provides a sample once every second as opposed to 50 times per second with the CW LIDAR.

The pulse shape for a pulsed system can usually be approximated by a Gaussian pulse,

$$I_n(r) = \frac{1}{\sqrt{\pi}r_p} e^{-\frac{(R-r)^2}{r_p^2}} \quad (2.14)$$

where R is the distance to the center of the range gate of interest and the e^{-1} width of the pulse, r_p , is given by

$$r_p = \frac{\Delta r}{2\sqrt{\ln 2}} \quad (2.15)$$

where Δr is the full-width-at-half-maximum pulse width [14]. Returns are integrated as the Gaussian pulse travels through the range gate volume according to the range weighting function

$$W(r) = \frac{1}{\Delta p} \int_{\frac{\Delta p}{2}}^{\frac{\Delta p}{2}} I_n(r+s) ds \quad (2.16)$$

where Δp is the size of the range gate. After integrating Eq. 2.16, in terms of the *Erf* function, the range weighting function for the range gate centered at a distance R away from the LIDAR is given by

$$W(r) = \frac{1}{2\Delta p} \left\{ \text{Erf} \left(\frac{r-R+\frac{\Delta p}{2}}{r_p} \right) - \text{Erf} \left(\frac{r-R-\frac{\Delta p}{2}}{r_p} \right) \right\}. \quad (2.17)$$

The pulsed LIDAR model in this report uses $\Delta r = 30$ m and $\Delta p = 30$ m. The first range gate is centered at a range of 35 meters and the last gate is centered at 275 meters, with range gates every 30 meters in between.

Figure 7 (a) compares RMS measurement error for forward staring CW and pulsed LIDARs at the 9 range gates used in the pulsed LIDAR model. The amount of error for the pulsed LIDAR remains constant for all range gates since the range weighting function does not change, and the minor variations visible are due to simulation imperfections. For ranges below roughly 135 meters the CW LIDAR measurements produce less error, and beyond 135 meters CW performs worse. Both technologies produce approximately the same amount of error at a range of 135 meters. Figure 7 (b) compares the range weighting functions for the two technologies at a range of 135 meters. The Gaussian-like shape of the pulsed weighting function has more of its energy concentrated in a smaller area while the CW weighting function has significant “tails” that contribute to spatial averaging far away from the intended range.

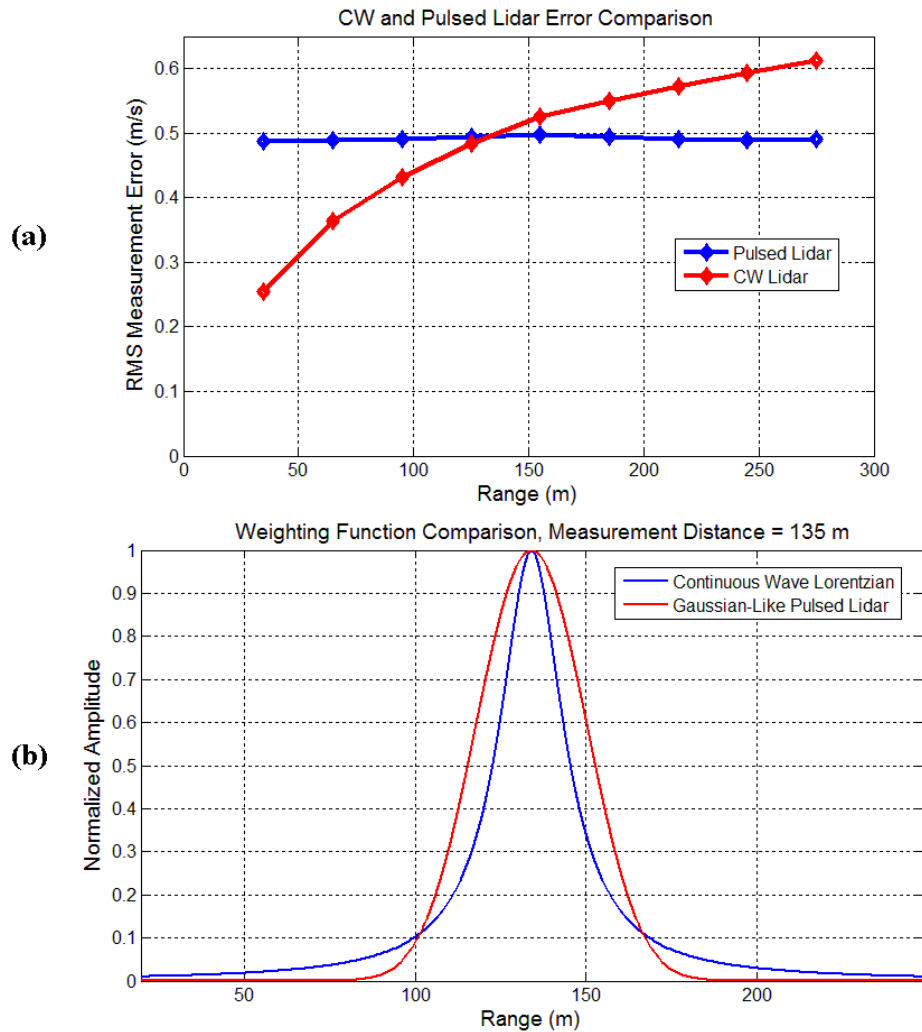


Figure 7. A comparison of CW and pulsed LIDARs based on parameters from commercially available LIDARs. (a) A comparison of RMS errors for a forward-pointing LIDAR configuration using the AR1 wind condition at ranges corresponding to range gates of a pulsed LIDAR. (b) A comparison of the pulsed range weighting function and the CW range weighting function at $F = 135$ meters.

The frequency response of the pulsed LIDAR range weighting function is provided in Figure 4 along with the CW frequency responses. Clearly the difference in the shape of the pulsed range weighting function results in a different spectral shape. If the range weighting functions are being described as low-pass filters, then the pulsed LIDAR filter has a much sharper transition between the pass band and the stop band and is therefore closer to an ideal low-pass filter.

3 LIDAR Simulation Results

Simulations were performed in FAST to assess the performance of CW and pulsed LIDARs in realistic preview measurement scenarios. All wind fields used were generated for use with a 5

MW turbine model with a hub height of 90 meters. RMS wind speed measurement errors were analyzed for a forward-pointing LIDAR ($\theta = 0$) at the hub location to assess the effects of range weighting alone for a variety of wind conditions. Ideal preview control systems might include LIDAR units mounted in the blades, so that preview measurements can be made in front of outboard sections of the blades, avoiding geometrical measurement errors. However, since a more economical and realistic method involves placing a single scanning LIDAR angled off of the x axis in the spinner of a turbine, spinning LIDAR performance was analyzed for different blade span positions and preview distances.

3.1 Wind Conditions

In order to test the performance of CW LIDAR in realistic wind environments, simulations were run using a variety of wind files generated with the Great Plains low level jet (LLJ) spectral model in TurbSim, characteristic of wind observed near Lamar, Colorado [12,2]. A library of wind files consisting of below rated (mean u component of wind speed $\bar{u} = 9$ m/s), rated ($\bar{u} = 11.4$ m/s), and above rated ($\bar{u} = 13$ m/s) conditions with various stability and friction velocity values was used for the simulations. A total of 31 wind fields, each 630 seconds in length were stochastically generated for each of the five varieties of wind conditions available at the three mean wind speeds. The wind files are sampled at 20 samples/second and contain 31 by 31 points in the yz plane. A summary of the library of wind files used is provided in Table 1. Although coherent structures have been generated to be superimposed over some of the wind files, the results in this section do not include coherent structures. U_{hub} indicates the reference streamwise wind speed, Ri_{TL} indicates the turbine layer gradient Richardson number, and α_D indicates the wind shear power law exponent. U_D^* is the average friction velocity, defined in Eq. (3.1), of wind at the hub, top of the rotor, and bottom of the rotor. $\overline{TI_U}$, $\overline{TI_V}$, and $\overline{TI_W}$ are the mean turbulence intensities of the u , v , and w components of wind speed, defined in Eq. (3.2), respectively. For the wind scenarios that do not have power law wind shears, jet height indicates the height of the center of the jet, which is at hub height for the 5 MW model.

Table 1. A Summary of the Great Plains Low Level Jet Wind Fields Used for Wind Speed Measurement Analysis

Simulation ID	U_{hub} (m/s)	Ri_{TL}	α_D	U_D^* (m/s)	$\overline{TI_U}$ (%)	$\overline{TI_V}$ (%)	$\overline{TI_W}$ (%)	Jet Height (m)
BR1	9	-0.1	0.123	0.399	6.61	8.14	6.33	N/A
BR2	9	0.02	0.235	0.341	8.00	7.47	5.68	N/A
BR3	9	0.2	0.273	0.135	3.61	4.71	2.73	N/A
BR4	9	0.02	N/A	0.29	7.07	6.68	4.97	90
BR5	9	0.2	N/A	0.158	4.26	4.90	3.08	90
R1	11.4	-0.1	0.086	0.451	6.31	7.15	5.82	N/A
R2	11.4	0.02	0.134	0.414	7.67	7.03	5.46	N/A
R3	11.4	0.2	0.365	0.149	3.62	3.47	2.56	N/A
R4	11.4	0.02	N/A	0.29	5.76	5.32	4.02	90
R5	11.4	0.2	N/A	0.158	3.61	3.54	2.56	90
AR1	13	-0.1	0.077	0.514	6.54	7.14	5.69	N/A
AR2	13	0.02	0.139	0.422	6.93	6.22	4.82	N/A
AR3	13	0.2	0.363	0.135	3.17	2.85	2.16	N/A
AR4	13	0.02	N/A	0.289	5.12	4.55	3.46	90
AR5	13	0.2	N/A	0.16	3.39	3.02	2.27	90

3.2 Impact of Turbulence on Measurement Errors

It is important to be able to judge the fidelity of wind speed measurements in a variety of wind conditions to determine when preview measurements will be reliable enough for use in control systems. RMS measurement error over an entire 10-minute wind field is used as a metric to compare LIDAR performance in this section. The amount of measurement error is not directly related to the mean wind speed of a wind field but rather to the turbulence parameters. For a forward pointing LIDAR at hub height, the wind shear profile will not affect wind speed errors either. Parameters that will likely impact range weighting errors are the Richardson number, defining vertical stability, the turbulence intensity (TI), and the local friction velocity, in m/s, defined as

$$u^* = \sqrt{|u'w'|} \quad (3.1)$$

where $u' = u - \bar{u}$ and $w' = w - \bar{w}$. Because range weighting acts as a filter on the wind field, another approach is to study the impact of range weighting for a variety of spectral shapes of the wind. In this research, this was not possible since all LLJ wind spectra, once normalized by some value, have roughly the same spectral shape.

The turbulence intensities of the three wind components, given by

$$\begin{aligned} TI_u &= \frac{\sigma_u}{\bar{u}} \\ TI_v &= \frac{\sigma_v}{\bar{u}} \\ TI_w &= \frac{\sigma_w}{\bar{u}} \end{aligned} \quad (3.2)$$

where σ_u , σ_v , and σ_w are the standard deviations of the u , v , and w wind speed components, respectively, are common ways of describing wind conditions [3] and are also easy to measure. The turbulence intensity value most commonly used to describe wind conditions is TI_u . Since it is actually the standard deviation of the wind that causes measurement errors rather than the turbulence intensity, the variable analyzed here is TI_u multiplied by the mean wind speed, or just the standard deviation of the u component, σ_u . Results showing the CW RMS errors between true wind speeds at the hub location and wind passed through range weighting filters are shown in Figure 8 as functions of σ_u .

Results for all 31 seeds for each of the 15 wind conditions are provided for a total of 465 wind conditions due to the fact that the various stochastic realizations of the 15 basic wind types have varying amounts of TI. While the results show that there is a general trend between σ_u and RMS error, it is clear that all seeds within one basic wind type produce roughly the same amount of error regardless of σ_u . At a focal distance of 200 meters, it appears that σ_u plays more of a role in determining RMS error. A possible reason for this is that at $F = 200$ m, the range weighting filter has a very low cutoff frequency of 0.0022 m^{-1} . Only turbulent features with wavelengths on the order of 450 meters or above are able to pass through the filter and it is likely that a TI value captures the low frequency fluctuations very well.

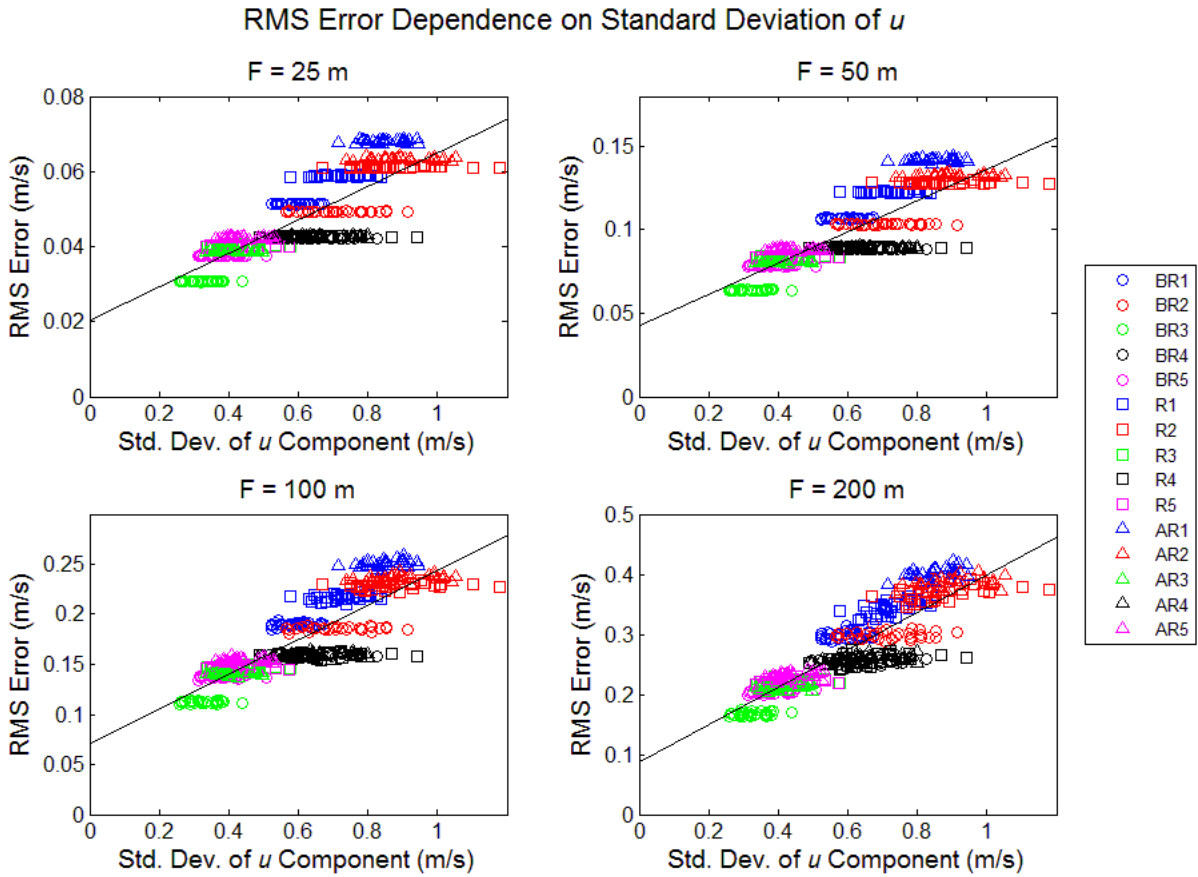


Figure 8. RMS wind speed measurement errors for a LIDAR pointed along the $-x$ axis at hub height for various focal distances as functions of standard deviation of the u component of wind speed. Results are shown for all 465 wind files generated for use with the 5 MW model.

Rather than treating standard deviation of wind speed as a reliable variable for estimating measurement error, a variable common to all of the realizations of a basic wind type is desired. Local friction velocity, or u^* , is a good figure for judging measurement errors because all seeds of a main wind type have the same local u^* values for the LLJ spectral model analyzed here. In fact, local u^* values control the scaling of the velocity spectra in the LLJ model.¹ In addition, u^* has been shown to be a good indicator of the number of high-loading events on a turbine [15,16] and may therefore be a useful value for analyzing the performance of a controller based on wind preview measurements. Results of RMS errors between true and measured wind for CW LIDAR are included in Figure 9 as functions of local u^* at hub height. It is important to note that the friction velocity referred to in this analysis is the local u^* at hub height rather than the average friction velocity over the entire rotor disk, U_D^* , shown in Table 1. Clearly, local u^* provides a much better indicator of forward-looking LIDAR performance, especially for the 25, 50, and 100 meter focal distances. When the LIDAR is focused at a distance of 200 meters, local u^* is still a reasonably good indicator of RMS error, but there tends to be more variation within a basic wind type. This is consistent with the results in Figure 8 that reveal an increasing dependence on σ_u for errors at greater focal distances.

¹ While the LLJ spectra scale with u^* , other spectral models such as the IEC models scale with σ_u .

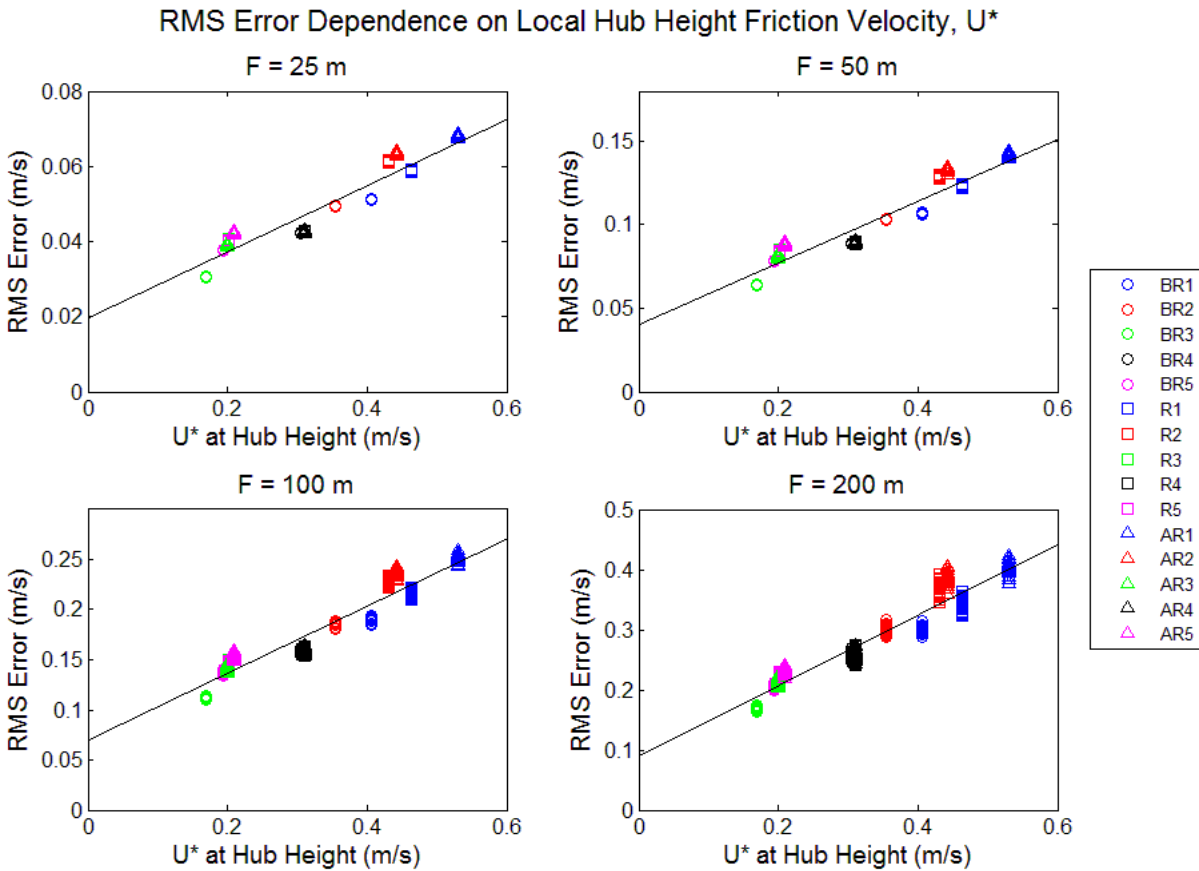


Figure 9. RMS wind speed measurement errors for a LIDAR pointed along the -x axis at hub height for various focal distances as functions of the local friction velocity u^* . Results are shown for all 465 wind files generated for use with the 5 MW model.

Pulsed LIDAR errors as a function of wind condition need to be analyzed for only one range, since the range weighting function does not change with measurement distance. Figure 10 shows pulsed LIDAR RMS error as a function of u^* and compares the trend with the CW results. The pulsed RMS errors are almost identical to the CW errors for a focal distance of 135 meters, as predicted in Figure 7. Pulsed and CW LIDARs focused at 135 meters provide the same amount of error as a function of u^* for a constant spectral shape of the wind. However, it is likely that overall RMS error for a pulsed LIDAR would be equivalent to CW error at some other focal distance for different spectral shapes of the wind due to the different shapes of the frequency responses for the pulsed and CW range weighting functions. For example, if the wind's spectrum was contained at frequencies very close to DC, the CW LIDAR focused at 135 meters would filter the wind more than the pulsed LIDAR, as seen in Figure 4, and would cause more measurement error. In this case, a CW LIDAR focused at a shorter distance than 135 meters would result in the same measurement error as the pulsed LIDAR.

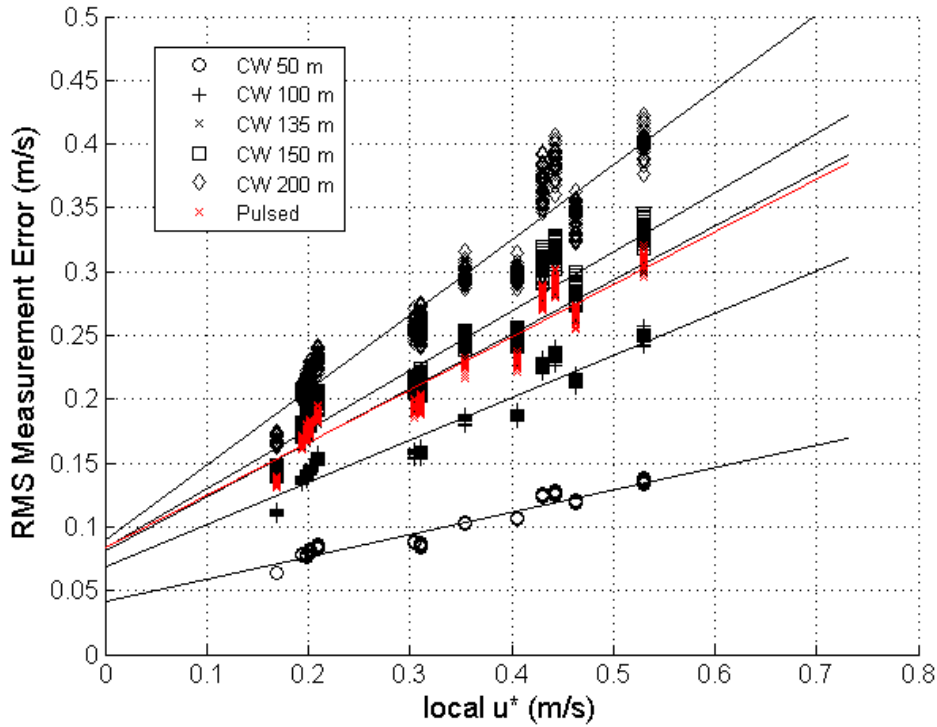


Figure 10. RMS wind speed measurement errors for a LIDAR pointed along the $-x$ axis at hub height for pulsed LIDAR and CW LIDAR at various focal distances as functions of the local friction velocity u^* .

3.3 Hub Mounted Spinning LIDAR Analysis

By mounting a LIDAR in the spinner of a wind turbine, the LIDAR can be offset at an angle θ and focused at a distance F so that measurements will be made at a radius r and a preview distance d in front of the turbine [see Figure 2 (b)]. In addition to the rotational rate of the turbine rotor, which may be too slow for the measurement rate desired, an additional rotational rate can be introduced. Since this method has been successfully tested on a 2.5 MW turbine [8], it is reasonable to assume that a likely measurement technique for a preview control implementation will involve a spinning LIDAR.

Observations based on the results in Figure 5 encouraged the study of “optimal” preview distances using CW LIDAR for specific scan radii, r , and wind conditions. For pulsed LIDAR there is no notion of an optimal preview distance yet, since error decreases monotonically with preview distance. The optimal preview distance is defined here as the distance for a given r that provides the lowest RMS measurement error while using a LIDAR mounted at the hub location. Although wind evolution would cause even more error between the measured wind speed and the wind speed that reaches the rotor, Taylor’s frozen turbulence hypothesis is assumed here, meaning that the optimal preview distance is judged based on measurement errors alone. In this report, RMS errors for a given r are calculated by averaging wind speed measurements at rotor angles $\psi = 0, 90, 180,$ and 270 degrees [see Figure 2(b)], the angles where measurements lie on wind field grid points for the chosen scan radii. We found that by modeling wind measurements on the TurbSim grid points, wind speeds more indicative of the intended turbulence conditions could be acquired. Measurement errors are shown as functions of preview distance for 14

different blade span radii in Figure 11 for the AR1 and AR3 wind conditions. The 14 radii analyzed correspond to the 14 sample locations along the y and z axes in the TurbSim file that are less than or equal to blade span. The AR1 wind type is the most turbulent of all wind types analyzed here, while AR3 represents relatively calm conditions. Figure 12 summarizes the minimum errors detected and the corresponding preview distances for the 14 blade span positions analyzed in Figure 11.

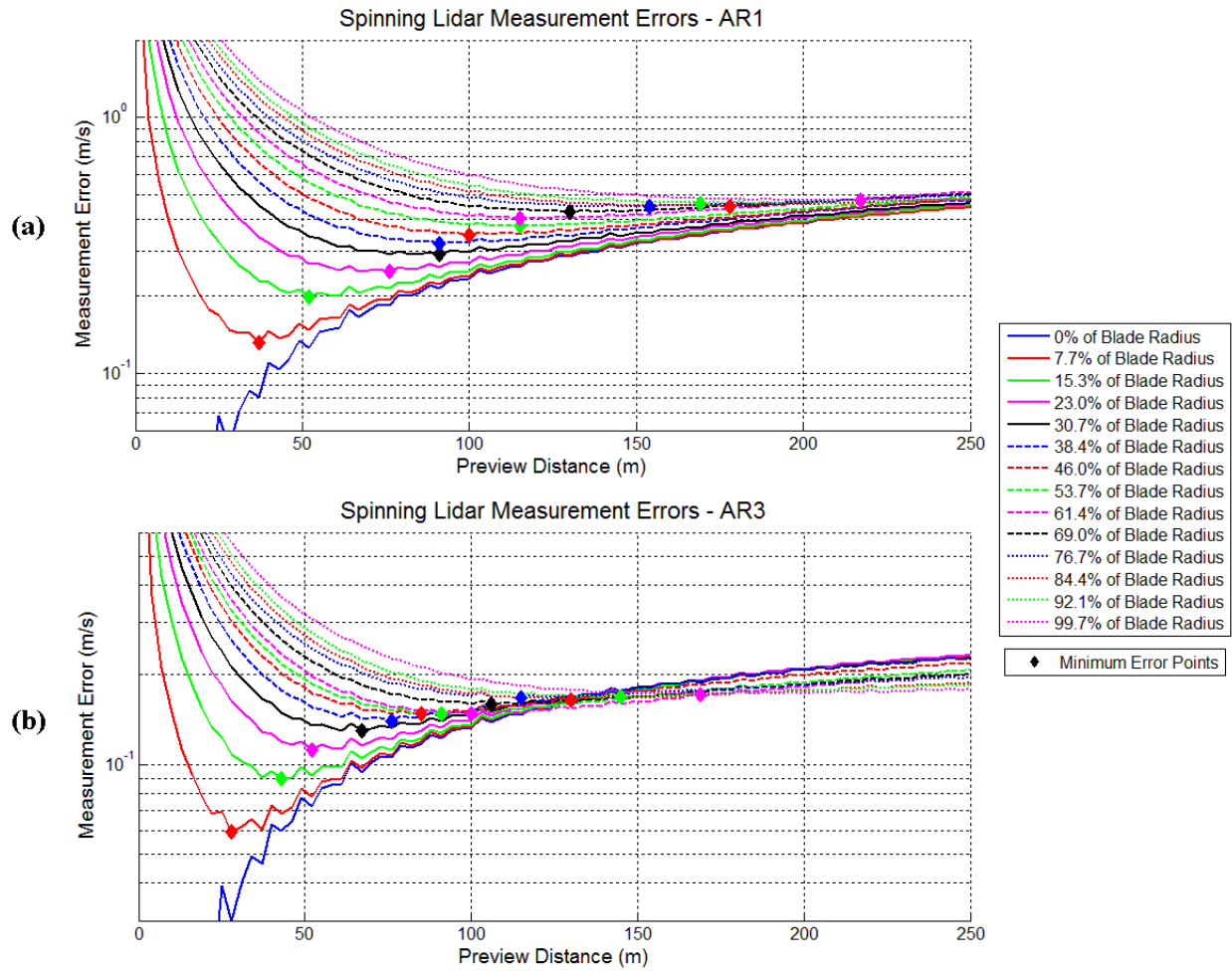


Figure 11. RMS measurement error as a function of preview distance for various scan radii, assuming a spinning LIDAR mounted in the spinner of a wind turbine. The optimal (minimum RMS error) preview points are plotted for each scan radii. (a) Results for the high turbulence AR1 wind type. (b) Results for the relatively calm AR3 wind condition.

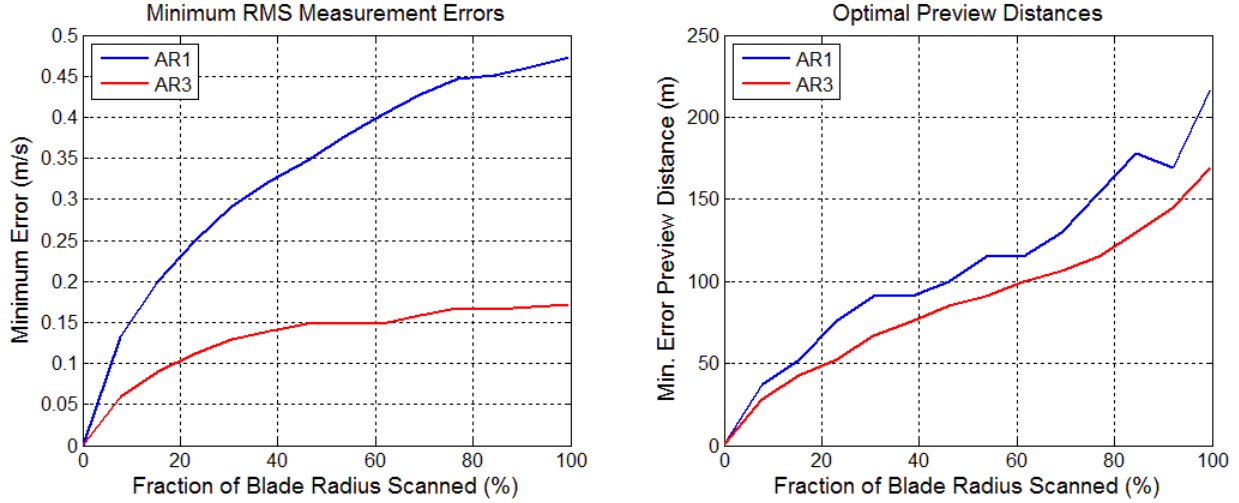


Figure 12. Optimal (minimum RMS error) measurement errors and preview distances corresponding to Figure 11 as functions of scan radius, r .

The optimal measurement distance can be roughly described as the point at which both geometrical errors and range weighting errors are low. For shorter distances measurement angle errors will cause error to increase, and for greater distances the low-pass filtering effect of range weighting will cause more significant error. The results of Figure 11 show that the optimal measurement distance is a strong function of r . As r increases, the optimal preview distance is greater because of the large measurement angle required to focus at a radius r . In addition, for the calmer wind condition, AR3, optimal preview distances tend to be closer to the turbine than for the AR1 case. In Figure 11 (a), one can see that for very large preview distances, all error curves tend to converge, because range weighting dominates over the low angular errors caused by very small θ .

Results for AR3 in Figure 11 (b) reveal a very interesting phenomenon. At great enough preview distances, measurements at smaller scan radii produce errors that are greater than those resulting from larger radii. This is a counterintuitive result because for a given preview distance larger scan radii should produce greater measurement errors, since θ is greater and the measurement angle errors have more of an impact. However, by observing how local u^* varies with height, some insight into this phenomenon can be gained. In Section 3.2, we found u^* to be a good indicator of the amount of measurement error that can be expected. Normalized profiles of u^* for AR1 through AR5 are shown in Figure 13. The ratio of u^* at 50% blade span above hub height to u^* at hub height, for example, is 0.62 for AR3, while it is 0.83 for AR1. This means that measurements at 50% blade span will be far less corrupted by turbulence compared to measurements at hub height for AR3 than they would be for AR1. Beyond a certain preview distance, for AR3, the decrease in range weighting error due to lower turbulence causes overall error to be lower for larger scan radii, even though the measurement angles are slightly greater. For AR1, the ratio between turbulence levels at hub height and larger blade radii is not great enough to counteract the increase in error due to greater measurement angles, θ . Therefore, the curves representing measurement error for small scan radii, r , in Figure 11 (a) do not eventually intersect and become greater than the curves corresponding to larger r , as they do in Figure 11 (b).

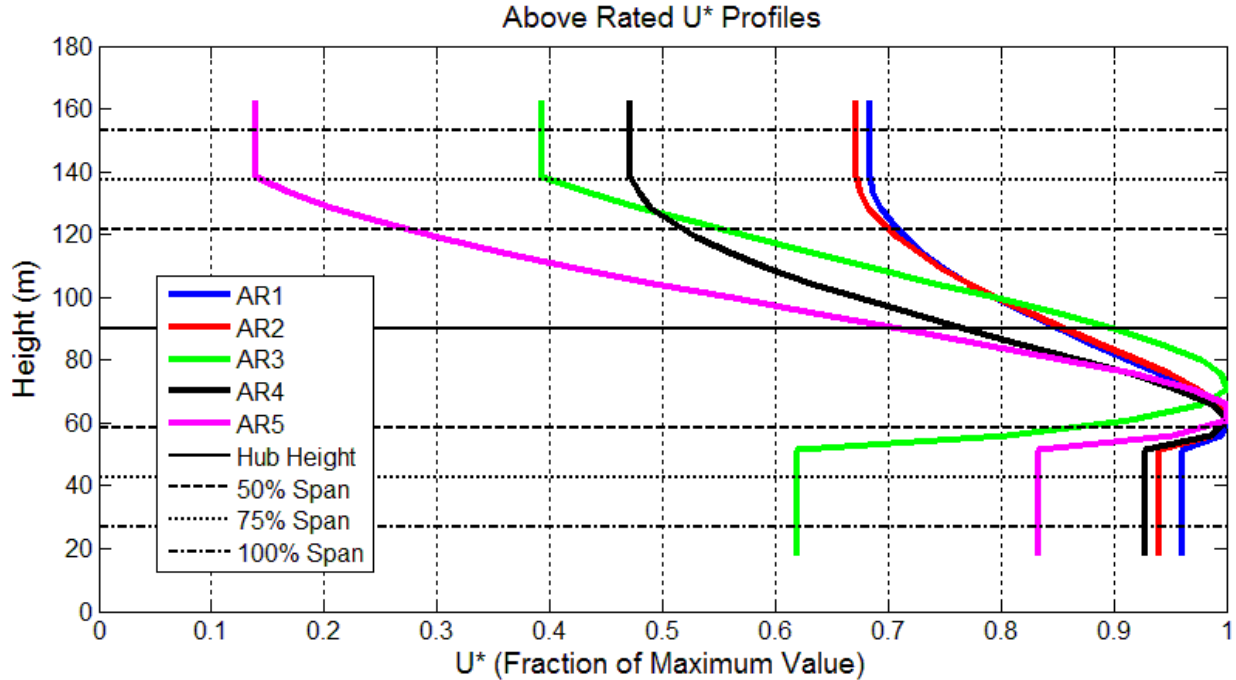


Figure 13. Height profiles of u^* for AR1 through AR5. All profiles have been normalized to their maximum value of u^* .

Previous LIDAR-based preview control studies have required knowledge of wind speeds concentrated heavily between 60% to 80% rotor radius [3] and at 75% rotor radius [1,2] because of maximum power extraction at these spans. To reflect the interest in wind speed measurements at these spans, simulations were performed for all 15 wind types for a scan radius of 75% blade span along with 50% and 100% blade span for comparison. Results from these simulations are included in Figure 14, which displays the average minimum measurement error achieved for each wind condition along with the preview distance at which the minimum error was measured. Minimum achievable RMS error is clearly a much stronger function of wind condition than optimal preview distance. For the high-interest 75% blade span scan radius, typical optimal preview distances for a variety of wind conditions are between 110 and 150 meters.

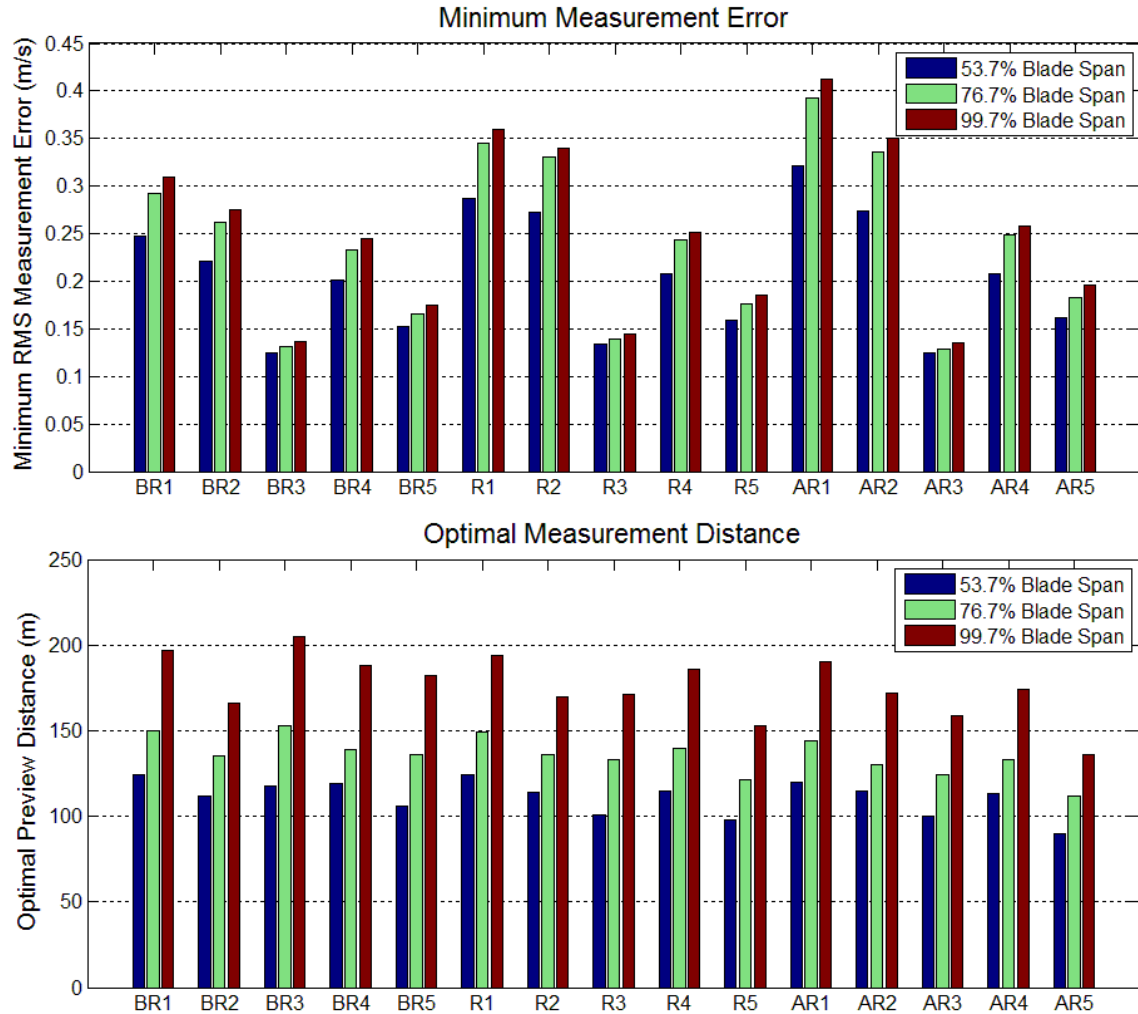


Figure 14. Minimum RMS measurement errors and corresponding optimal preview distances for measurements using a spinning LIDAR located at the hub of a wind turbine for scan radii of 53.7%, 76.7%, and 99.7% blade span (33.83 m, 48.33 m, and 62.83 m, respectively). The scanned radii correspond to the grid points closest to 50%, 75%, and 100% blade span containing wind speed samples in the TurbSim files.

In order to assess how pulsed LIDAR measurements would perform compared to CW, error as a function of preview distance is shown for the AR1 wind category for pulsed and CW LIDARs in Figure 15 for 50%, 75%, and 100% blade span. There are three regions in the plot worth noting. The first region is for very short preview distances where errors are high but pulsed measurements perform slightly better than CW measurements. The second region is for moderate preview distances. Here, CW LIDAR performs better because its range weighting function filters out less wind energy than the pulsed weighting function. The third region is for large preview distances. In this region, pulsed LIDARs produce less error because the CW range weighting functions have become wide enough to filter out more wind components than the pulsed weighting functions. The second and third regions are expected. It is the first region that contains counterintuitive results.

One would expect CW to perform better in the first region because of the relatively short focal distances and therefore insignificant range weighting. However, at these close preview distances, the main source of error is the wind component in the yz plane (see the Appendix), and this source is reduced slightly more with wider range weighting functions. The estimate of the desired u component of wind assumes that v and w are zero and a wide weighting function will spatially average these components more than a narrow weighting function. Since v and w are zero mean, by averaging the wind speed vectors over a wider area, they will be reduced more and will cause the u estimate to contain more accurate assumptions. For short distances, the wider pulsed weighting function is reducing the contributions from v and w enough to produce slightly lower overall errors than the CW LIDAR.

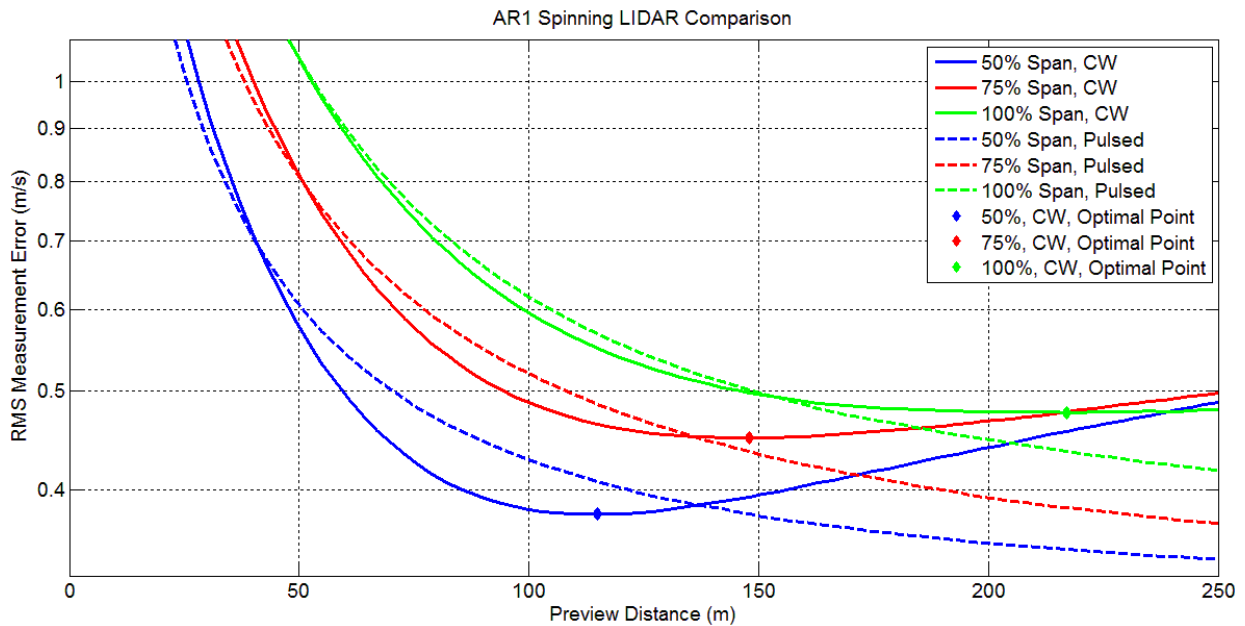


Figure 15. RMS measurement error as a function of preview distance for the high-turbulence AR1 wind type. Results are shown for CW and Pulsed LIDAR.

It is worth noting that the results shown in Figure 15 were generated assuming the measurement range of the pulsed LIDAR could be continuously varied and that the sample rate was as high as that of the CW LIDAR. In reality, the slower sampling rates of pulsed LIDARs may make them undesirable for spinning LIDAR applications due to the spatial averaging that occurs as the LIDAR measurement point moves along an arc while returns are integrated (see Eq. 2.13).

4 LIDAR Modeling Conclusions and Future Work

This section of the report has provided an analysis of the application of continuous-wave (CW) and pulsed Doppler LIDARs to preview wind measurements on a wind turbine. The analysis has specifically focused on the two main sources of error during LIDAR measurement, including range weighting and geometrical errors, and the measurement scenarios where each source is dominant. Figure 5 and Figure 6 suggest that measurement angles greater than 45 degrees should be used with caution because of the large errors introduced by the relatively strong v and w components of radial velocity. The local friction velocity, u^* , was shown through simulation to provide a good indication of the amount of wind speed measurement error due to range

weighting. An analysis of a realistic hub mounted spinning CW LIDAR measurement scenario for a 5 MW turbine was made, with results revealing the preview distances that one might expect to provide the minimum RMS error for specific scan radii. Initial results for wind preview based feed-forward controllers utilizing the CW LIDAR model developed in this study are documented later in this report and in Dunne *et al.* [17] and Laks *et al.* [18].

On-going work involving CW LIDAR modeling includes investigating random LIDAR errors due to optical and electronic noise. Measurement noise likely varies with turbulence conditions and a model of noise is desirable in a future LIDAR model. A thorough analysis of measurements of coherent structures, such as Kelvin-Helmholtz billows, in the wind fields is needed. Studies have shown that coherent structures cause severe turbine loads [15], and it is a goal of wind preview-based controllers to mitigate the loads caused by coherent structures. Therefore, it is essential to determine the fidelity that LIDAR measurements of coherent structures can achieve.

Initial results have illustrated the problems that can be caused by coherent turbulence events and an example of the large measurement errors that can be caused is provided in Figure 16. Figure 16 (a) shows the turbulent wind field in the xz plane ($y = 0$), without the mean u component of 13 m/s, from the AR4 wind type with a superimposed coherent structure. The measurement scenario used to assess the measurement errors is shown as well. A LIDAR is focused at hub height at a range of 100 meters and an angle of 30° . Figure 16 (b) shows the measurement errors corresponding to the x measurement locations at hub height in (a). It can be seen that the coherent structure introduces very strong positive w wind components around hub height that last for about 200 meters in the x direction. Due to the measurement geometry these coherent positive w components cause a lower line-of-sight velocity to be measured by the LIDAR. The result is that the measured and estimated u value is much lower than the actual u component, with a peak underestimation of 2.5 m/s.

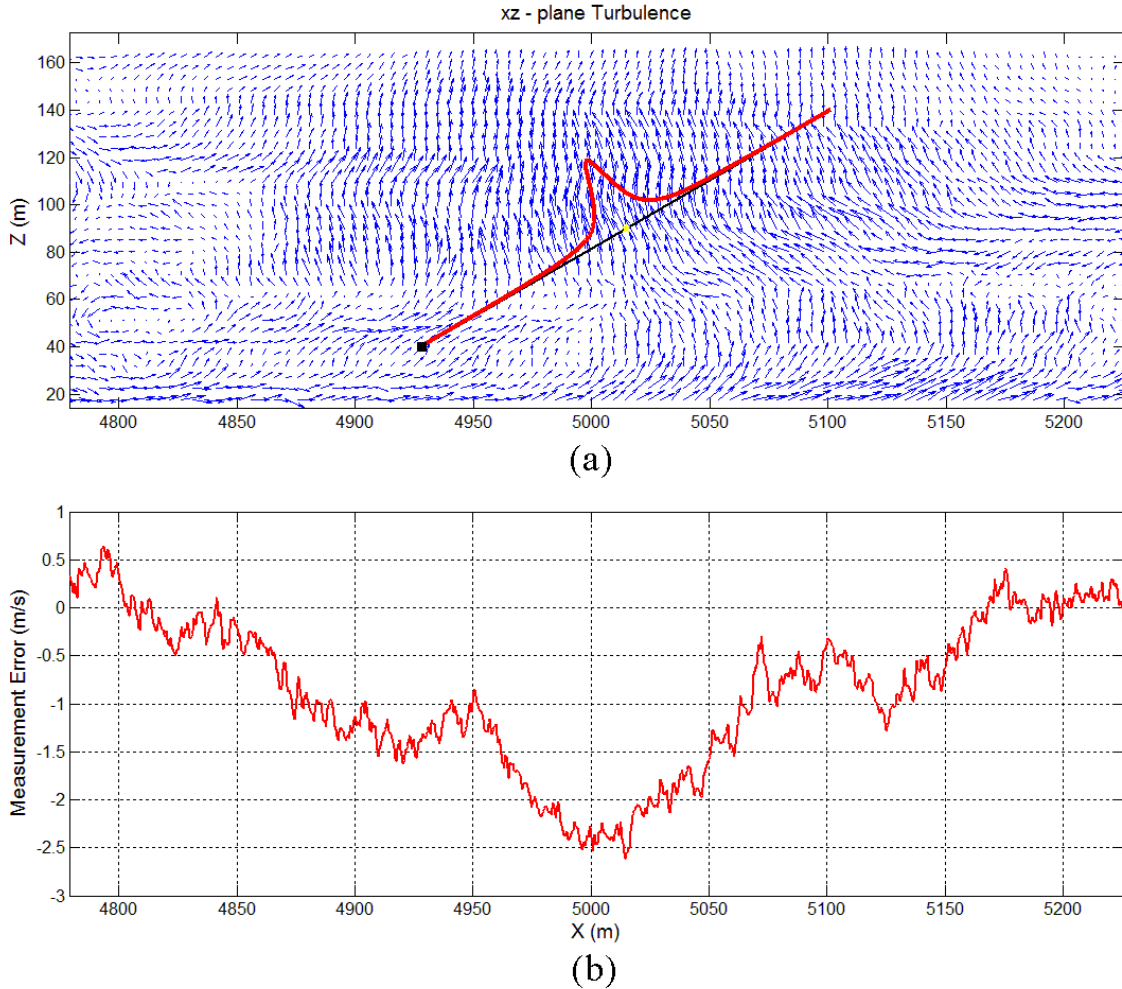


Figure 16. An example of a coherent structure causing severe wind measurement error. (a) The wind field, with the mean u wind speed of 13 m/s subtracted, in the xz plane containing a superimposed coherent structure. (b) Wind speed measurement errors caused by a CW LIDAR measuring the wind field in (a) at hub height at an angle of 30° with a focal distance of 100 meters.

As shown in Figure 1, wind evolution presents another source of wind preview uncertainty that was not discussed in this work. Future efforts in wind evolution modeling and simulation are required to fully assess the effectiveness of LIDAR wind preview measurements for control applications. An implication of the studies in this report is that it may be impractical for a LIDAR unit based in the spinner of a wind turbine to provide accurate wind preview measurements at large scanning radii close to the turbine. To avoid measurement errors due to geometry, one possibility is to measure the wind farther away from the turbine and delay the measurements before they are input to a controller if the controller requires very short preview times [1]. We anticipate that with the addition of wind evolution modeling, optimal preview distances such as those shown in Figure 12 and Figure 14 will no longer be valid because wind evolution will cause shorter preview distances to be favored, since wind evolves more over greater distances. As a result, it may be difficult to provide highly accurate preview measurements to a controller using a hub mounted spinning LIDAR. More simulations using

LIDAR and wind evolution models are required to fully understand the capabilities of LIDAR-based wind preview measurements.

5 Feed-Forward Control Introduction

Current commercial wind turbine control algorithms are feedback only, as shown in Figure 17. Blade pitch is often controlled by a simple proportional-integral (PI) based collective blade pitch controller, which receives its input signal from the error in generator speed. Recent work [19,20,21,22] has verified that more advanced feedback controllers can reduce structural fatigue loads. These advanced controllers typically employ individual pitch control and may be based on signals from strain gauges and position encoders in addition to generator speed.

LIDAR can be used to remotely measure wind speed. Recent improvements in LIDAR size, cost, and reliability have made it realistic to obtain accurate wind speed measurements upstream of the turbine [8]. When wind speed measurements are available, it is possible to use this additional information through disturbance feed-forward control. This feed-forward control can be combined with either standard or advanced feedback control, as shown in Figure 18. The use of these wind speed measurements to reduce turbine fatigue loads is an area that is being actively researched [1,2,3,6,7].

In this study, a feed-forward controller is added on to a standard feedback controller, and the results are compared to the standard feedback controller alone. A previous study [2] investigated the same configuration, but with different feed-forward control designs: model-inverse and shaped compensators. The best of these previous designs, with perfect wind measurements, resulted in blade root and tower fore-aft load reductions between 5% and 15%, but slightly increased tower side-to-side motion.

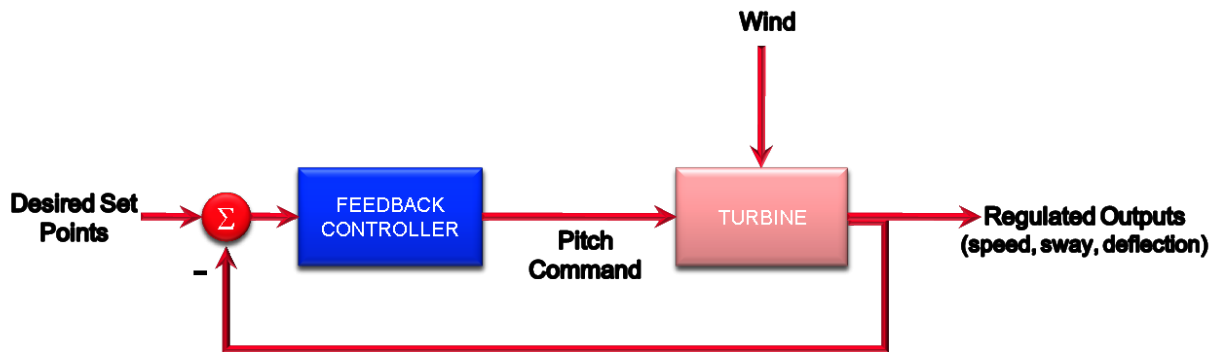


Figure 17. Feedback only control

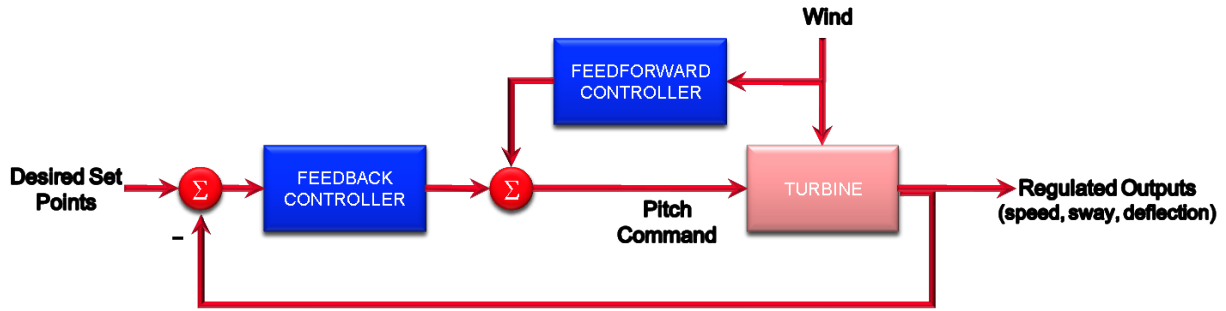


Figure 18. Combined feedback/feed-forward control

6 Simulated Turbine and Turbulent Inflow

6.1 5 MW Turbine Model and Baseline Control

All simulations are performed using a full non-linear turbine model provided by the FAST [9] software code developed at NREL. The particular model used in FAST is the NREL 5 MW reference turbine [10]. All available degrees of freedom (DOFs) except teeter are turned on in simulations. The baseline collective pitch controller is a gain-scheduled PI control [10].

An individual pitch feedback-only controller was also designed [19] for use as another baseline controller for comparison with individual pitch feed-forward controllers. In addition to generator speed, its inputs are the three out-of-plane blade root bending moments, and the rotor azimuth, which is used for the multi-blade coordinate (MBC) transformation [23]. The horizontal and vertical components are controlled with PI controllers, and the collective component is controlled with the same PI feedback control as the baseline collective pitch controller.

For all simulations, a 2nd-order pitch actuator model has been added to the 5 MW turbine model, with a natural frequency of 1 Hz and a damping ratio of 0.7. After FAST is used to find a linearized model of the turbine, this pitch actuator model is also added on to the linear model. FAST linearization is performed with a constant torque, while actual Region 3 operation has a varying torque to maintain rated power. Therefore the linear model is also modified to account for this varying torque by augmenting it with a generator speed-to-torque feedback linearized at the operating point. This overall model, shown as P in Figure 19, is then used for design.

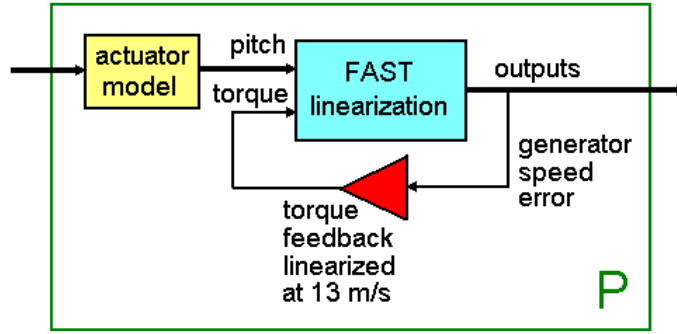


Figure 19. Linear plant model used for control design. The linear turbine model from FAST is augmented with an actuator model and linearized torque feedback.

6.2 Wind Fields

The wind fields used in simulation are described by rows AR1, AR2, and AR3 from Table 1. These turbulent fields all have a 13 m/s mean hub-height wind speed and are representative of the Great Plains region. The first 99 sec of each 630 second simulation are discarded before calculating any performance measures to allow initial transients to settle out. Two of the realizations in particular, AR2_s1 and AR2_s13 (seed 1 and seed 13 of subpopulation AR2) will be referred to later in this report.

7 Non-Causal Series Expansion

7.1 Design

Non-causal series expansion is a model-inverse method not tested in the previous study [2]. A first step in designing a linear model-inverse feed-forward controller is obtaining a linear model of the turbine (P). In this study, the turbine is linearized with five degrees of freedom turned on: first flapwise blade mode (for each of the 3 blades), drivetrain rotational-flexibility, and generator. This is performed using the linearization capability of FAST [9] to create a state-space model of the turbine based on perturbations from a particular operating point.

From the state-space model, two transfer functions are extracted: $P_{ob_{cmd}}$ maps collective blade pitch error b_{cmd} to the error o in some output to be regulated; P_{ow} maps deviation from nominal wind speed w to the output error o . Then a linearized version of the baseline feedback control is connected to this state-space model of the turbine, resulting in two closed-loop transfer functions: T_{ob} maps collective blade pitch feed-forward input b to the error o in some output to be regulated. T_{ow} maps deviation from nominal wind speed w to the output error o .

A feed-forward controller is shown as F in Figure 20. A linear model-inverse feed-forward approach uses F to cancel the effect of w on o . Therefore, as can be seen in Figure 20,

$$T_{ob} \cdot F \cdot w = -T_{ow} \cdot w$$

$$F = -T_{ob}^{-1} T_{ow}$$

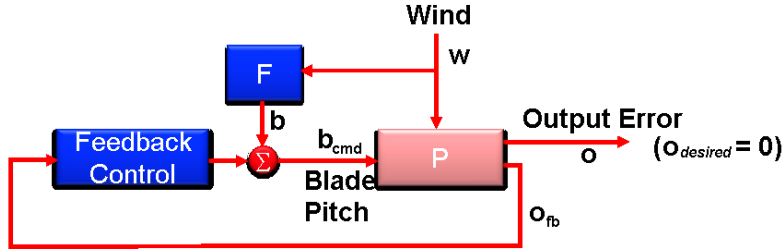


Figure 20. Combined feedback/feed-forward control, labeled to illustrate a linear model-inverse feed-forward approach

In the special case when $o = o_{fb}$ (e.g., when the output of interest is generator speed error, the same output used in the collective-pitch feedback loop), it turns out that the closed-loop transfer functions T_{ob} and T_{ow} each differ from their corresponding open-loop transfer functions in the same way, so that $F = -T_{ob}^{-1}T_{ow} = -P_{ob_cmd}^{-1}P_{ow}$, and it doesn't matter whether the open-loop or closed-loop transfer functions are used. However, when $o \neq o_{fb}$, it is important to use the closed-loop transfer functions when determining F .

Ideally, the feed-forward controller would be set equal to F as above. However, in this case the resulting F is unstable because T_{ob} contains non-minimum phase zeros. Therefore a stable model-inverse approximation is used instead.

In the previous study [2], three different model-inverse techniques [24,25,26,27] were investigated: nonminimum-phase zero ignore (NPZ-Ignore), zero-phase-error tracking control (ZPETC), and zero-magnitude-error tracking control (ZMETC). These worked well when controlling a linear plant model, but performed worse than the baseline controller alone when simulated in FAST with the full nonlinear wind turbine dynamics. This study investigates a different model-inverse approximation method: non-causal series expansion (NCSE) [28,29]. NPZ-Ignore is actually a zeroth-order NCSE, but this study addresses higher orders of NCSE. This type of inversion requires the most preview time and should theoretically provide a better approximate inverse than the NPZ-Ignore, ZPETC, and ZMETC methods.

The NCSE method results in a stable approximate model-inverse by using a Taylor series approximation. For example, if the desired F contains an unstable pole a , then we replace $\frac{1}{z-a}$ with $-\left(\frac{1}{a}\right) - \left(\frac{1}{a}\right)^2 z - \left(\frac{1}{a}\right)^3 z^2 \dots$ which is stable, but non-causal. For each term included in the approximation, an additional sample of preview is required.

Other improvements were also made in addition to changing the approximate inversion method. The three previous model-inverse controllers [2] were designed to regulate the generator speed output, with the hope that they would also reduce structural loads. This NCSE control is instead directly designed to regulate the blade root bending moment output. The previous controllers were based on a model linearized about an operating point of 18 m/s wind speed and were gain scheduled, while this NCSE control is linearized at 13 m/s to better match simulation conditions

and is not gain scheduled. Low-pass filtering was also treated differently; the original design had one low-pass filter on the linear feed-forward controller, and a different low-pass filter on its gain-scheduling multiplier. The new design has no gain-scheduling multiplier, but instead has two parts described below, each with a different low-pass filter. Finally, the wind speed measurement used by the feed-forward control in previous simulations was an average of five points taken at the hub and outer edges of the rotor plane. In this study, it is an average of three points, one at 75% span of each blade, since accounting for tip losses, the blades are most sensitive to wind speed around this span location [3].

The NCSE control was first tested on the linear model for three varying parameters: approximation series order, sample rate used in conversion to discrete time, and number of DOFs turned on in linearization. Greater approximation series orders, sample rates, and number of DOFs were expected to improve performance, but they also increased the occurrence of numerical problems. We attempted to compare these different design options using the \mathcal{H}_2 norm from wind speed error to root bending moment error, but numerical problems with Matlab's [30] `norm()` function appeared with higher orders of approximation. Careful choice of system representation in Simulink was also required to avoid numerical problems, with the feed-forward controller split into a transfer function portion and a zero-pole-gain portion. The following choices were made in the design: approximation order = 199, 80 Hz sample rate, and 5 DOFs in linearization. This resulted in a 2.5 sec preview time (200 samples: 199 from the approximation order plus 1 because the 5 DOF model had 1 non-minimum phase zero [28]).

This NCSE feed-forward control does not need to operate at very low frequencies, because the focus is more about minimizing fluctuations in root moment, and less about the steady-state value. On the other hand, steady-state rotor speed is very important. Therefore the overall feed-forward control is the sum of a high-pass filtered NCSE control and a low-pass filtered rotor speed control, as shown in Figure 21. Both filters have a 3 dB point at 10^{-2} Hz, since wind begins to affect rotor speed relatively less than root bending moment above this frequency. The wind speed input to the rotor speed feed-forward control signal (upper path in Figure 21) can also be delayed compared to the NCSE feed-forward control signal (lower path in Figure 21), since only the NCSE control was designed to have a 2.5 second preview. The rotor speed control uses a simple lookup table, with values based on testing of the non-linear turbine model at various operating points over a range of wind speeds from 11.4 to 25 m/s to find the required steady-state blade pitch at each operating point such that rated rotor speed is maintained. The feedback controller is still working to control rotor speed as well.

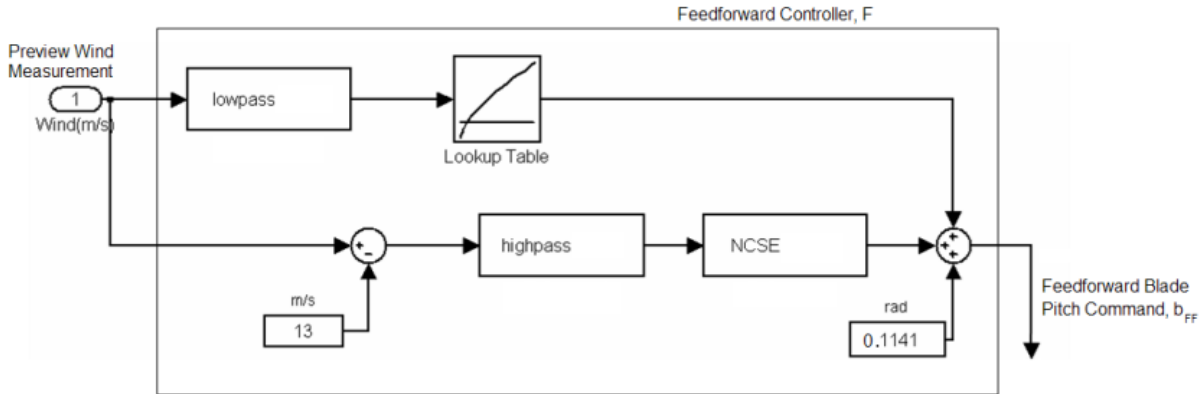


Figure 21. Feed-forward control combining rotor speed regulation at low frequencies (upper path) and NCSE root bending moment reduction at higher frequencies (lower path). The linearization operating point is at 13 m/s wind speed and 0.1141 rad (6.537 degrees) blade pitch.

7.2 Results

The non-causal series expansion controller was simulated in both individual pitch and collective pitch form. In the individual pitch version, there are three copies of the feed-forward controller, one controlling each blade. Three perfect point wind speed measurements are taken, 2.5 seconds ahead of each blade at 75% span, and these are fed into their respective feed-forward controllers. This individual pitch feed-forward control is then added on to the individual pitch baseline feedback controller. Results shown here are for the individual pitch version simulated in wind field AR2_s1; the collective pitch version had similar results.

Structural loading measures include RMS nacelle velocities and damage equivalent loads (DELs) of blade and tower bending moments. DELs are calculated using code from NREL based on a rainflow counting algorithm [31] also used in the NREL code CRUNCH and the Sandia code LIFE2, with a Wohler curve exponent of 10, typical for composite material.

Figure 22 shows that the NCSE controller does reduce blade root bending loads as designed, but also causes unacceptable increases in RMS nacelle velocity. Various other configurations of the NCSE control were also simulated considering different low-pass and high-pass filters, different preview lengths to each path of the controller, only one or the other path of the controller, etc. However, no configuration produced results that were clearly better overall than the individual pitch baseline feedback controller. Simulations were done in wind field AR2_s1, using perfect point wind measurements. Peak pitch rates were 0.81, 2.63, 7.23, 7.96, and 2.60 degrees/sec, respectively, for the five methods whose results are summarized in Figure 22. All controllers produced an average power of 5000.0 kW. Based on the plotted performance measures, the combined shaped feed-forward IP compensator augmented to the baseline IP feedback controller [2] remains the best overall controller, even compared with the new NCSE feed-forward compensators augmented to the baseline IP feedback controller.

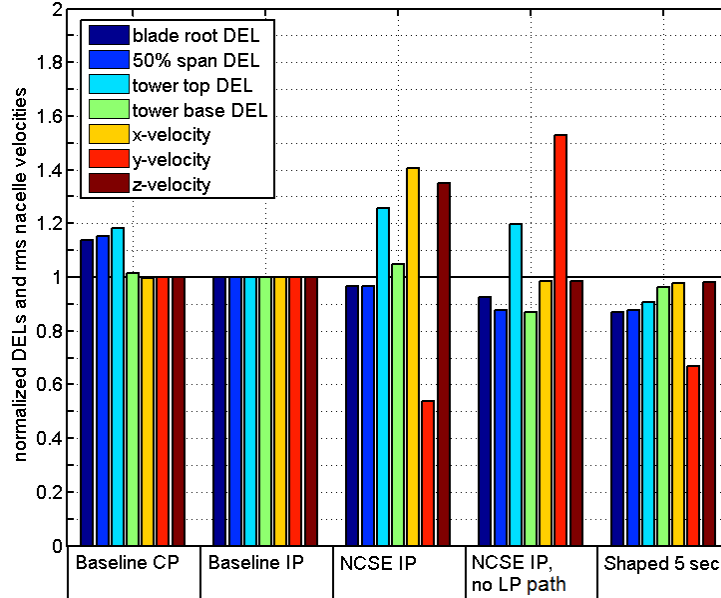


Figure 22. A comparison of damage equivalent loads (DELs) and nacelle RMS velocities for the baseline collective pitch (CP) feedback-only controller, the baseline individual pitch (IP) feedback-only controller, the non-causal series expansion (NCSE) individual pitch (IP) feed-forward controller augmented to the baseline IP feedback controller, the same NCSE controller without the lowpass (LP) filtered rotor speed control path, and the shaped IP feed-forward compensator with 5s preview and IP feedback (best of previous work [2]). All results are normalized to the Baseline IP results.

8 Preview Control

Preview Control [32] is a method that incorporates a preview of the wind speed disturbance and includes a cost function that allows explicit minimization of rotor speed error, loads, and pitch rate.

8.1 Design

The particular version of Preview Control used in this study is one that is designed to be added to a predetermined feedback controller, which in this case is the baseline collective-pitch PI controller. Given a linear turbine model, predetermined feedback PI gains, weights for the cost function, and the desired number of preview samples, Preview Control allows researchers to solve for a feed-forward controller that minimizes the cost, given a step change in disturbance (wind speed).

Initially, Preview Controllers were designed to minimize only rotor speed error and pitch rate. On both the linear model and in nonlinear simulation, these designs reduced blade root loads in addition to rotor speed error, but increased tower fore-aft motion compared to the baseline controller. Therefore, the procedure was modified so that the rate of change of nacelle fore-aft velocity could be included in the cost function: the weighting matrix used (on the right side of equation 17 in the solution in [32]) is changed from the originally intended

$$- \begin{bmatrix} Q & 0 \\ 0 & 0 \end{bmatrix}$$

to

$$- \begin{bmatrix} Q & 0 \\ 0 & W_S \end{bmatrix}$$

where Q is a $n_o \times n_o$ matrix, weighting the error e in the n_o outputs (just generator speed in this case), and W_s is an $n \times n$ matrix, weighting the rate of change of the n plant states x . This changes the cost function from

$$J = \sum_{k=0}^{\infty} e^T(k) Q e(k) + [\Delta u_{fp}(k)]^T R [\Delta u_{fp}(k)]$$

to

$$J = \sum_{k=0}^{\infty} e^T(k) Q e(k) + [\Delta u_{fp}(k)]^T R [\Delta u_{fp}(k)] + [\Delta x(k)]^T W_S [\Delta x(k)]$$

where R is a weighting on actuator rate Δu_{fp} (pitch rate in this case).

The initial design was based on a 5 DOF turbine model (generator, drive train torsion, and first blade flap for each of the 3 blades), linearized about a wind speed of 13 m/s, and augmented with the actuator model and torque control feedback. The revised design instead has all DOFs (including tower bending) included in the linear model. The baseline PI feedback control is gain scheduled, so the gains at the 13 m/s linearization point were used: $K_p = 9.68e-4$ and $K_i = 4.15e-4$. The weights chosen were: $Q=1$ (generator speed error), $R=10^4$ (pitch rate), and $W_s = 10^5 C^T C$ (tower sway) where C is a row vector that returns the fore-aft nacelle velocity when multiplied by the column vector of plant states. The number of preview samples chosen was 396, requiring 4.95 seconds of wind preview (very close to the ‘‘Shaped 5s’’ controller, which actually has 4.96 seconds of preview).

Figure 23 shows the pulse response for the Preview Controller with varying preview lengths. These pulse responses show what the pitch angle command would be for a discrete unit impulse in wind speed at time 0. If the pulse responses of two linear controllers are the same, then the controllers are the same. Pulse responses that are non-zero before time 0 require preview measurements. In the initial design, additional preview does not have much effect beyond about 2 seconds of preview. This can be seen in Figure 23 because the blue, green, and red lines all overlap and match each other very closely. (The pulse response is 0 at any time where it is not shown.) But when the design is revised to include tower sway, additional preview continues to have an effect up until about 30 seconds of preview. However, a preview length of 4.95 seconds was chosen instead. Thirty seconds was deemed too large because the longer the preview time, the farther ahead of the turbine the LIDAR must be focused, increasing errors due to wind evolution and spatial averaging by the LIDAR [33]. However, focusing too close to the turbine can also cause errors, as discussed in the first part of this report. If the LIDAR is mounted on the turbine hub or nacelle, and scanning ahead of the turbine around a circle with a radius equal to

75 % of the rotor radius, its angle θ relative to an axis pointing into the wind will increase as the LIDAR measurement is taken closer to the turbine. The LIDAR measures wind speed in its line-of-sight direction, and wind speed is estimated in the downwind direction, assuming the non-downwind components of wind speed are zero. In practice, since the non-downwind components of wind speed are not always zero, errors increase as this angle θ increases. For the 5 MW turbine considered and wind measurements of 75 % span, a LIDAR angle of 30 degrees corresponds to 82 meters ahead of the turbine, which gives a preview time of 3.3 to 7.2 seconds in the rated-to-cut-out range of 11.4 m/s to 25 m/s. The chosen preview length of 4.95 seconds falls in this range.

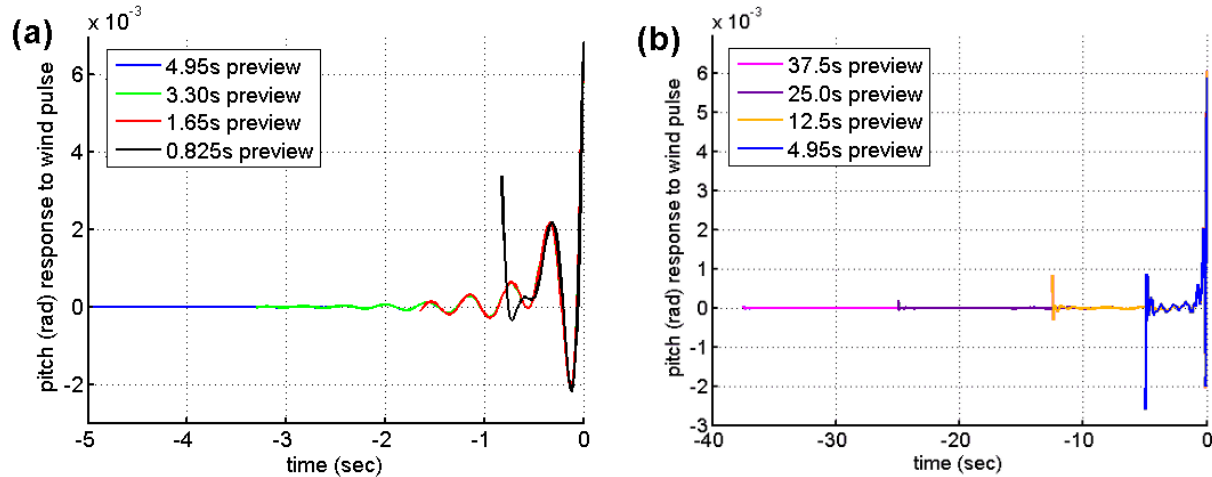


Figure 23. Preview Control pulse responses for varying preview lengths (shown in different colors) for (a) the initial 5 DOF design and (b) the revised design with tower sway included in the cost function. The blue line in (b) is the final design used.

8.2 Results

Figure 24 and Figure 25 show that the preview controller works as designed on the linear model, reducing the effect of wind disturbance on rotor speed error as well as blade and tower loads. Additional testing on the linear model also demonstrates that the Preview Controller is still beneficial with a 1/8 second error (delay or advance from the designed 4.95 seconds) in preview time, and that performance degrades to worse than baseline control alone when errors in preview time become greater than 1/2 second.

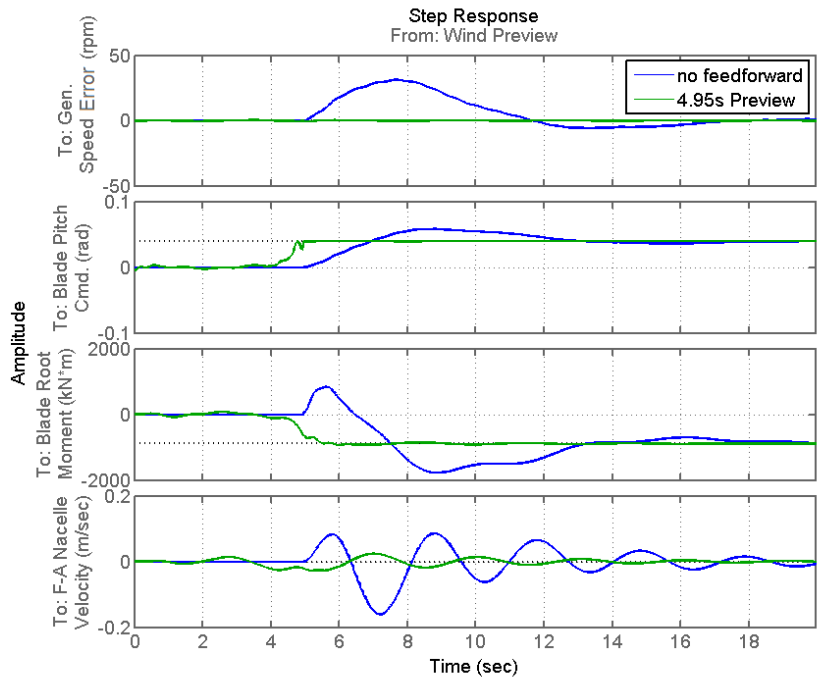


Figure 24. Linear turbine model response to a step change in wind speed hitting the turbine at 4.95 seconds, comparing Preview Control to no Preview Control.

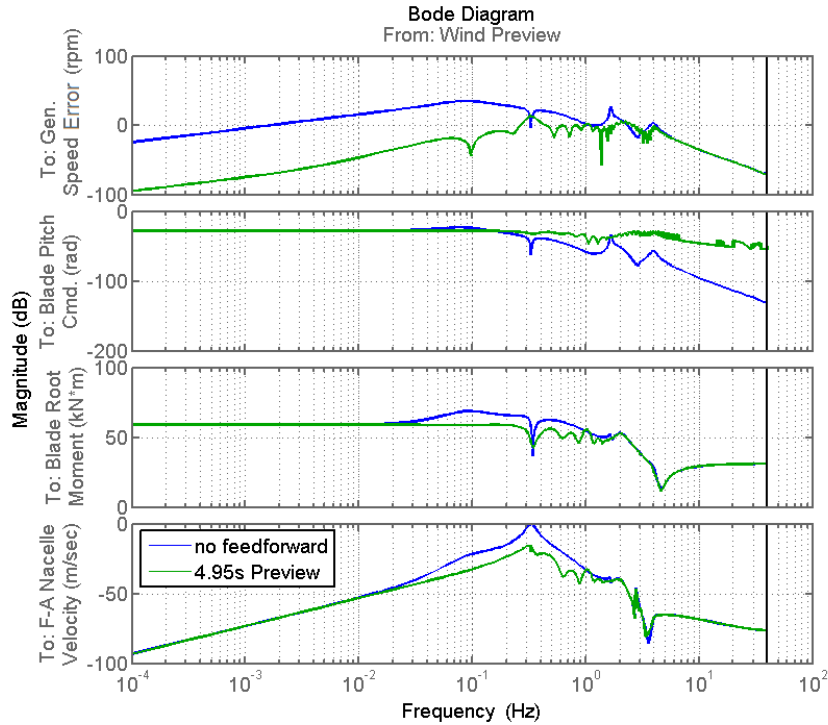


Figure 25. Bode magnitude plot of linear turbine model showing that Preview Control improves rejection of wind speed disturbances. This shows reduced generator speed error, increased blade pitching, and reduced blade root moment and fore-aft nacelle velocity.

In simulation, the Preview Controller was implemented in collective pitch form, with wind speeds measured 4.95 seconds ahead of the three blades at 75% span and averaged together for the feed-forward control input. When simulated in simple uniform wind fields, Figure 26 and Figure 27 show that the Preview Controller is still working to reduce the rotor speed error as well as blade and tower loads on the nonlinear turbine model, although there is some loss in performance. However, when simulated in a turbulent wind field, tower fore-aft motion is worse with Preview Control, as shown in Figure 28 and Figure 29. Initial investigations of IP Preview Control produced similar results to the CP Preview Control shown, and IP Preview Control may be investigated further in the future.

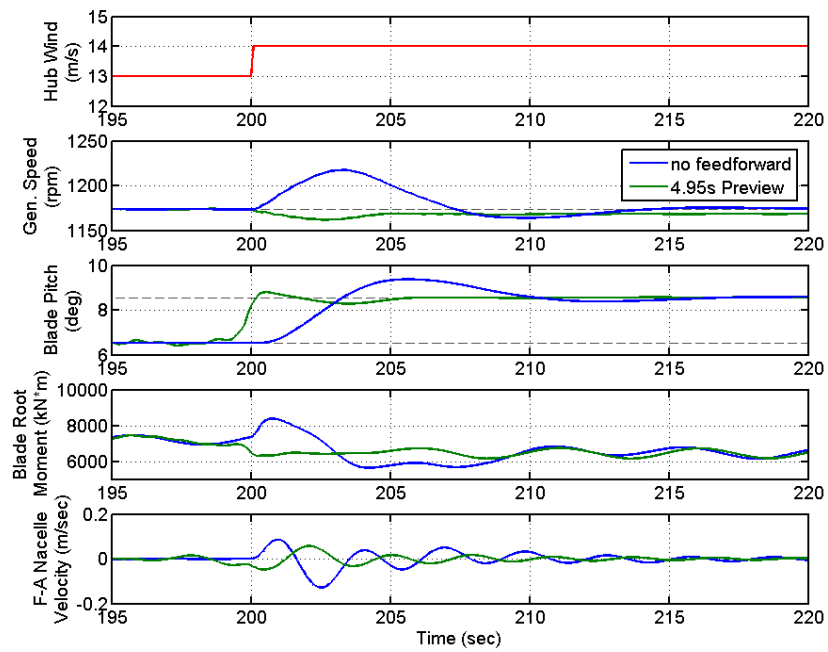


Figure 26. Simulated nonlinear turbine model response to a step change (from 13 m/s to 14 m/s) in uniform wind speed hitting the turbine at 200 seconds, comparing Preview Control to no Preview Control.

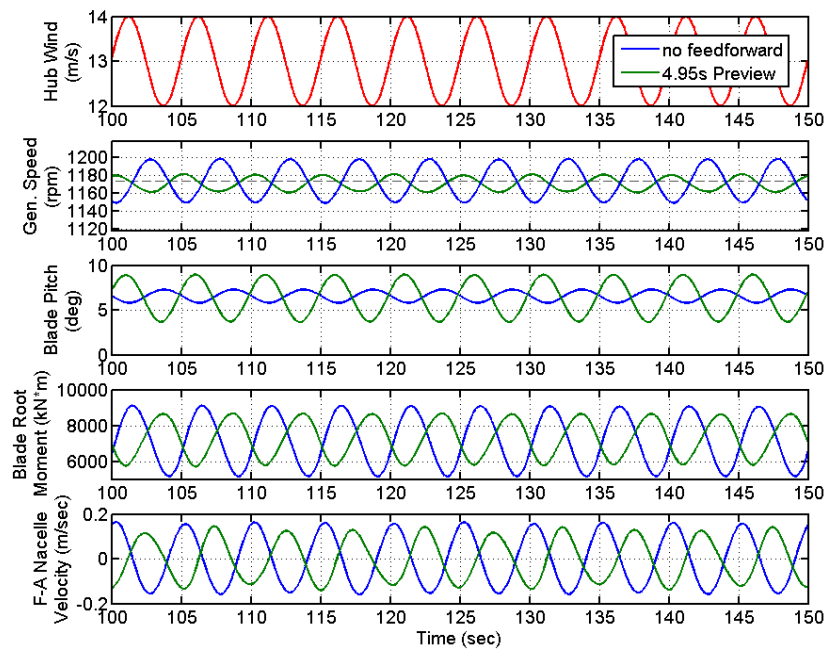


Figure 27. Simulated nonlinear turbine model response to a sinusoidal uniform wind speed with a period of 5 seconds, comparing Preview Control to no Preview Control.

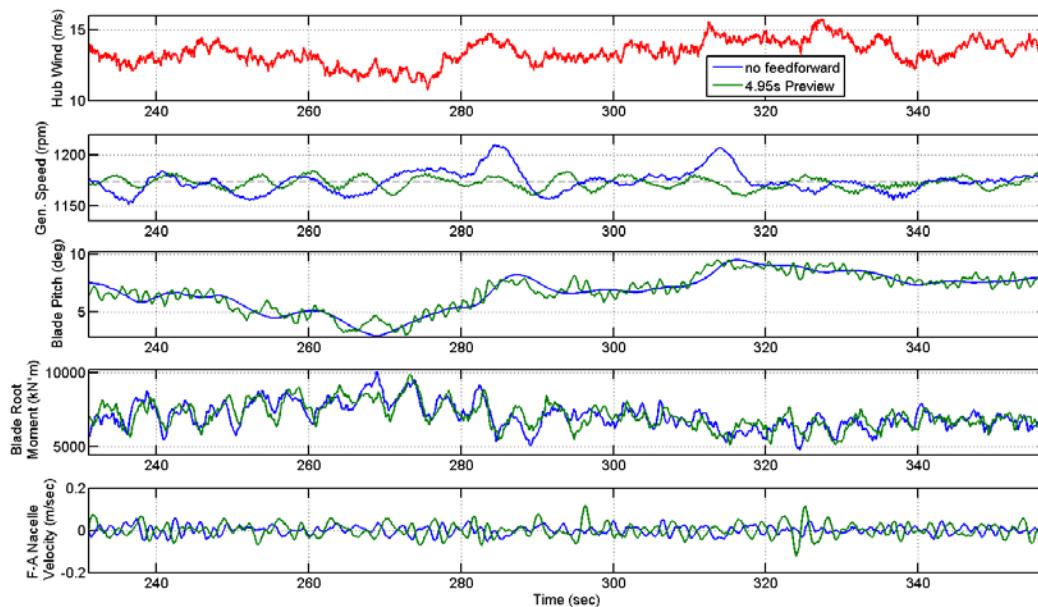


Figure 28. Time series comparing baseline collective pitch feedback control with and without Preview Control in wind field AR2_s1. The lowest plot shows increased tower motion with Preview Control.

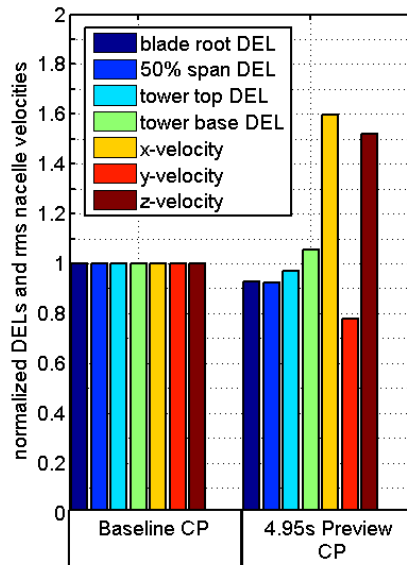


Figure 29. A comparison of damage equivalent loads (DELs) and nacelle RMS velocities for the baseline collective pitch (CP) controller and the CP 4.95 second Preview Controller in wind field AR2_s1. Peak pitch rates were 0.81 and 4.60 degrees/second, respectively. Both controllers produced an average power of 5000.0 kW. Results are normalized to the Baseline CP results.

9 Optimized FIR Filter

9.1 Design

Many of the previously mentioned feed-forward designs can be represented as finite impulse response (FIR) filters with discrete-time transfer functions with all poles at zero. Given an input of a unit pulse in wind speed, the FIR filter is described by its finite output sequence. For example, the pulse responses of the controllers described above are shown in Figure 30. In this figure, the amplitudes have been scaled for this comparison so that all controllers have the same DC gain, because different controllers were originally designed at different operating points and therefore different DC gains. Time 0 is when the wind pulse hits the turbine. The Shaped 10/3s feed-forward controller [2] has a pulse response that begins and ends 10/3s before and after time 0. Similarly, the Shaped 5s begins and ends 5s before and after time 0. The NCSE controller response, although it looks very small everywhere except near time 0, actually begins 2.5s before 0 and continues indefinitely. The Preview Controller response begins 4.95 seconds before 0, and ends at 0.

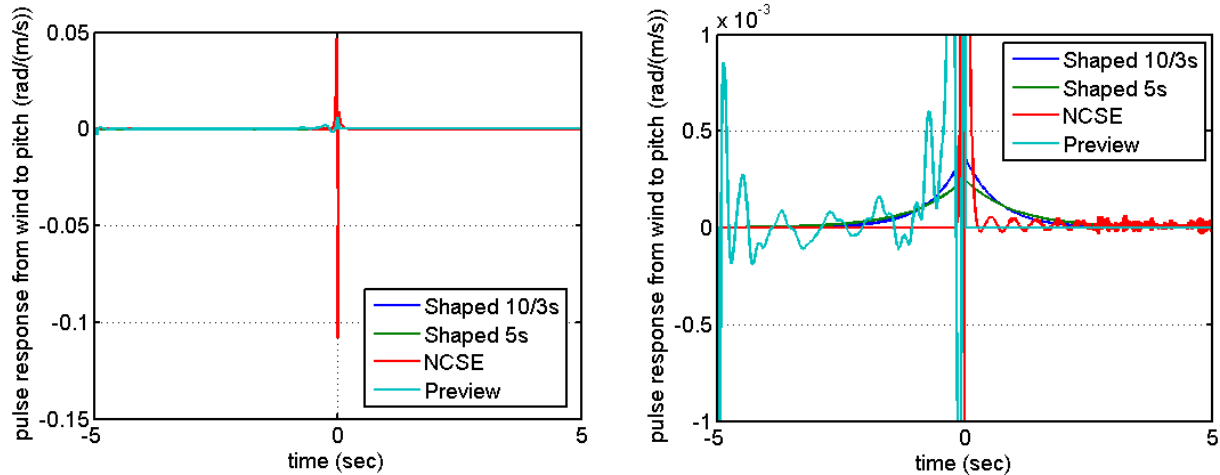


Figure 30. Pulse responses of various feed-forward controllers from previous and current studies (right plot is a zoom-in of the left plot).

For the optimized FIR filter, a sample time of 0.0125 seconds and a total response length of 10 seconds were chosen. Its input is wind speed with a preview time of 5 seconds. This filter is therefore characterized by a sequence of 800 pitch command gain values, which all need to be optimized. The optimized FIR filter was found using a genetic algorithm [34], which simulates thousands of random possible FIR filters, converging on combinations of those with the best simulation results. Performance was based on fatigue load reduction (blade and tower damage equivalent loads and nacelle accelerations), RMS pitch rate, peak rotor speed, and average power achieved in a simulation of the nonlinear turbine, with all DOFs, in above rated wind conditions. Wind field AR2_s13 from the previous study [2] was used for these simulations because it was shown that it produced the highest blade root loads out of all AR wind fields.

This genetic algorithm optimization approach is advantageous because it optimizes the controller directly on the nonlinear turbine model in a turbulent wind field, with LIDAR errors modeled, whereas feed-forward controllers designed based on a linearized turbine model with uniform wind fields often perform poorly in nonlinear turbulent simulations. The algorithm was seeded with the best of previous feed-forward designs, ensuring that results will be at least as good as previous designs on wind field AR2_s13.

The optimization was performed using the Genetic Algorithm function of the Matlab Optimization Toolbox [30]. To reduce the number of variables that need to be optimized by the algorithm, the FIR sequence is down sampled to 81 points instead of 800, with heaviest sampling near 5 sec (since there will be a 5 sec preview time, this corresponds to time 0 in Figure 30, where the most detail is required). For simulation, the full sequence of values was interpolated. After interpolation, the DC gain of the FIR filter is scaled to 1. This scaled FIR filter is then placed in series with a lookup table that converts from steady-state wind speed values to the corresponding steady-state blade pitch values.

Three copies of this feed-forward controller are then implemented, one controlling each blade. Three wind speed measurements are taken, 5 seconds ahead of each blade at 75 % span, and fed

into their respective feed-forward controllers, giving us individual pitch control. This feed-forward control is then added on to the individual pitch baseline feedback controller.

While the previous controllers used wind speed measurements that were perfect point measurements, here wind speed measurements that incorporate a CW LIDAR model [33] are used. It includes spatial averaging, which is significant at the preview distance that is used ($5 \text{ sec} \times 13 \text{ m/s} = 65 \text{ m}$). We also assume three hub-mounted LIDARs spinning at a cone angle θ of about 35 degrees. A LIDAR can only measure wind speed in its line-of-sight direction, which is at a 35-degree angle from the horizontal downwind direction in this model. Thus, the wind speed in the horizontal downwind direction can only be estimated. To make this estimate, it is assumed that the vertical and crosswind wind speed components are zero. Therefore, by using the LIDAR model, measurement angle errors are included as well as spatial averaging errors in the wind speed measurements.

9.1.1 Cost Function

The genetic algorithm attempts to find the filter with the minimum cost. This cost is calculated as the sum of the following eight performance measures, after each has been normalized by the corresponding value for an individual pitch baseline simulation: DELs on blade root, tower-top fore-aft, tower-base fore-aft, and shaft; RMS values of nacelle acceleration in the x , y , and z directions; and RMS pitch rate. This sum is then divided by 8, so that a cost < 1 represents better performance than IP baseline, and a cost > 1 is worse. Further, if rotor speed and power requirements are not met, the cost is increased sharply, as shown in the following pseudocode:

if $PeakRotorSpeed > 13$ (rpm), then $cost = cost \cdot (1 + (PeakRotorSpeed - 13) \cdot 10)$

if $AveragePower < 4999.9$ (kW), then $cost = cost \cdot (1 + (5000 - AveragePower) \cdot 10)$

9.1.2 Constraints

To reduce the amount of time required for the algorithm to run, the set of possible filters to evaluate was reduced to those most likely to produce good results. First, the slope of the impulse response was constrained to be no more than 0.0002 rad/sample, because based on experience from initial tests, FIR filters with large impulse-response slopes returned high costs. For example, the Preview Controller returned a higher cost than the baseline individual-pitch controller when evaluated with the cost function described above. If no limit is placed on slope, the individual FIR filters that the algorithm creates all tend to have very high slope. Second, the algorithm requires an initial range, so the values of the impulse response were limited to between -0.01 and 0.01 radians, since the well-performing shaped controller impulse responses fell within this range. Both of these constraints are imposed before the DC gain is scaled to 1.

9.1.3 Seeds

The genetic algorithm was seeded with the following FIR filters: Shaped 10/3 second and Shaped 5 second. These shaped compensators had the best results in previous work [2]. The NCSE and Preview Controllers were not used as seeds. The NCSE controller has an infinite impulse response. While it could be approximated as an FIR filter, its impulse response is significant out to 100 seconds, and begins to cause computer memory problems if stored in FIR form at this length. The Preview Controller impulse response contains steep changes in pitch that do not meet the slope constraints indicated above.

9.1.4 Creation Function

The genetic algorithm begins by creating a random initial population of individual FIR filters to evaluate. Starting with this initial population, the best (lowest cost) individuals in each generation are used as “parents” for the next generation, where they are randomly mutated and combined with each other. We chose to begin with an initial population size of 1000. Because we already had 2 seeds, this left 998 individuals that needed to be created before running the genetic algorithm. The Matlab Optimization Toolbox comes with a creation function, but using this creation function with our chosen constraints resulted in 998 individuals that looked almost exactly the same. Therefore we created a custom creation function to create individuals more randomly. These more adequately spanned the space of possible impulse responses. This custom creation function was based on the Matlab function `linprog()`. This is a linear programming function that outputs the vector x that minimizes $f^T x$, subject to constraints, where the vector f is an input. To create each of the 998 individuals, we ran `linprog()` using an input f that was randomly generated, and used the output x as a new individual. The result was that each individual x was random and also met our chosen constraints.

9.2 Results

On wind field AR2_s13, the lowest cost for a FIR filter returned by the genetic algorithm was 0.924. This is the result of about four weeks of simulation time. This cost represents an overall load reduction of about 8% compared to IP baseline. Figure 31 and Figure 32 show the impulse response and Bode magnitude plot of this best performing FIR filter. In the impulse response, the general shape of the Shaped 5 second feed-forward controller can still be seen, along with additional spikes. The Bode magnitude plot shows that the feed-forward gain decreases with frequency, and has already decreased significantly at the fairly low frequency of 0.1 Hz.

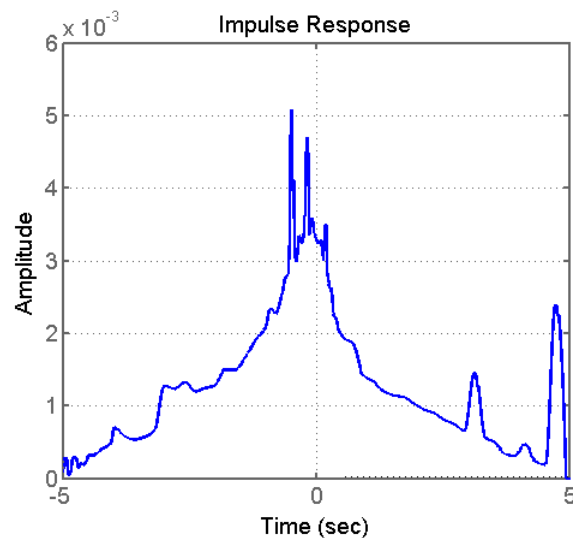


Figure 31. Impulse response of the Optimized FIR filter. Its cost on wind field AR2_s13 is 0.924.

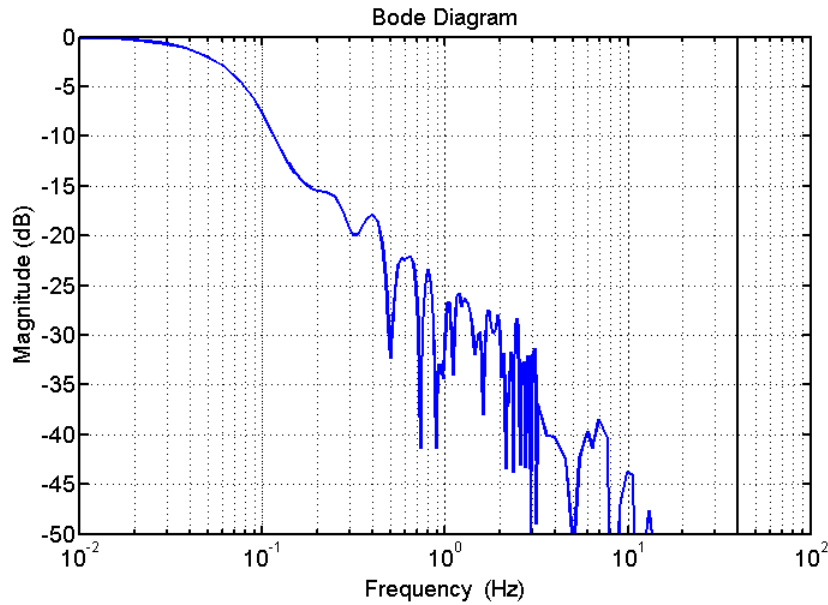


Figure 32. Bode magnitude plot of the Optimized FIR filter. Its cost on wind field AR2_s13 is 0.924.

Optimized FIR filter results should be at least as good as the best feed-forward controllers so far, since these were used to seed the optimization algorithm. However, error in wind speed measurement is also being introduced through a CW LIDAR model, so overall load reduction is not as high as before. For comparison, the Shaped 5 second controller seed returned a cost of 0.99.

The best controller on wind field AR2_s13 (shown in Figure 31 and Figure 32) was also tested on all of wind fields AR1 through AR3 and compared to the IP baseline controller alone. On 15 of these 93 wind fields, running the IP baseline controller alone results in an average power of below 4999.9 kW. Therefore, it no longer makes sense in the cost function to penalize the feed-forward controller for power below 4999.9 kW. With this part of the cost removed, the average cost for the optimized feed-forward controller over AR1 through AR3 is 0.945. None of the runs resulted in any rotor speed above 13 rpm, so the cost is based solely on structural loading and pitch actuation and represents an average of 5.5% load reduction. The average power over all wind fields was 5000 kW, both with and without the optimized FIR feed-forward controller. Figure 33 shows how the 5.5% average cost reduction is broken down among the eight different measures.

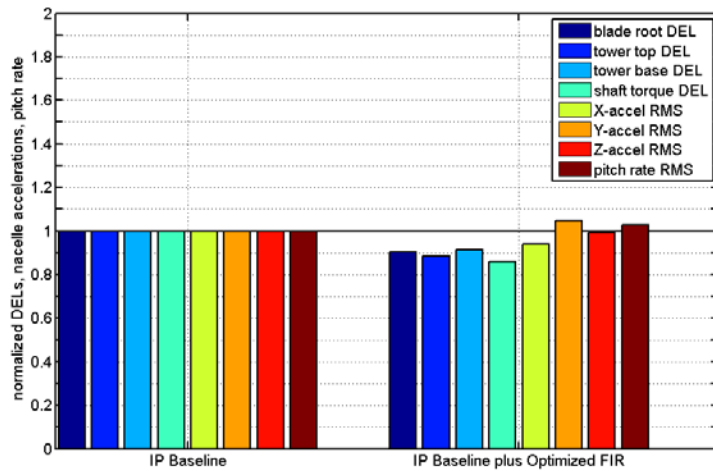


Figure 33. Damage equivalent loads, RMS nacelle accelerations, and RMS pitch rate of IP baseline control without and with optimized FIR feed-forward (using 5 second preview from three rotating LIDAR wind measurements). Values are shown relative to IP baseline alone, and are averaged over 93 wind fields (AR1, AR2, AR3). The optimized FIR's overall cost of 0.945 is the average of its eight bars.

This optimized FIR filter was also tested on wind fields AR4 and AR5 from Table 1. These wind fields include coherent structures. Results are shown in Figure 34. When results are averaged over all of AR1 through AR5, loads are reduced by 5%.

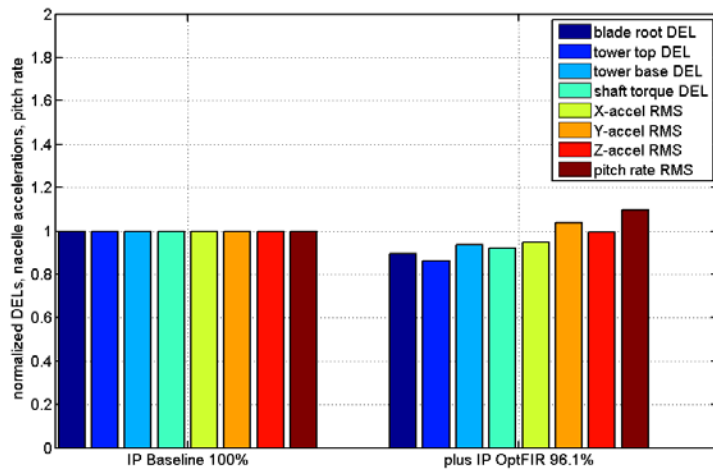


Figure 34. Damage equivalent loads, RMS nacelle accelerations, and RMS pitch rate of IP baseline control without and with optimized FIR feed-forward (using 5 second preview from three rotating LIDAR wind measurements). Values are shown relative to IP Baseline alone, and are averaged over 62 wind fields (AR4, AR5). The optimized FIR's overall cost of 0.961 is the average of its eight bars.

10 Feed-Forward Control Conclusions

Three feed-forward blade pitch control designs have been investigated and evaluated: non-causal series expansion, Preview Control, and optimized FIR filter. The non-causal series expansion controllers reduce blade loads, but increase tower sway, and are overall not an improvement over baseline individual pitch control. NCSE and other model-inverse methods are designed to reduce the effect of wind disturbances on only one choice of output. However, it is advantageous to control several outputs, including rotor speed, blade bending, and tower sway. In addition, model-inverse design methods result in feed-forward controllers with high gain at high frequencies, and also do not account for actuator limits, and so the pitch command reaches the 8 degree/second rate limit when using NCSE control and other model-inverse methods tried. For these reasons, Preview Control was investigated, which minimizes a cost that can include multiple outputs and actuator effort.

Preview Control was able to reduce both blade and tower loads on the linear model as well as in simple uniform wind field simulations. However, when simulated in turbulent wind conditions, like the NCSE control, Preview Control increased tower sway and was not an overall improvement over baseline control.

There are nonlinear approaches to model-inverse control [35], and possibly also to Preview Control, but since linear controllers have implementation and analysis conveniences, we investigated the optimized FIR filter as another linear control design. The optimized FIR filter was designed directly on the nonlinear turbine model in turbulent wind conditions with LIDAR errors modeled. It reduced loads on different parts of the turbine by varying amounts, with an average 5% load reduction overall, while maintaining rated power and rotor speed and without significantly increasing pitch rate.

11 Overall Conclusions and Future Work

This study focused on the use of a hub-mounted LIDAR for feed-forward wind turbine controls. The two major sources of LIDAR measurement error studied were spatial averaging and measurement angle error. On the 5 MW turbine model with a hub-mounted spinning CW LIDAR, when measuring wind speeds at 75% span, the minimum RMS error occurred between about 100 and 150 meters ahead of the turbine, depending on the local friction velocity of the wind. Once wind evolution error is also included, it is expected that this optimal measurement distance will decrease. Therefore, using a preview distance of 65 meters, various feed-forward blade pitch controllers were designed to reduce turbine loads. The best simulation results were from the optimized FIR controller. When this individual pitch feed-forward controller was added to a baseline individual pitch feedback controller, the average load reduction over a set of eight different turbine components was 5%, compared to individual pitch feedback alone. Future investigations will study random LIDAR noise errors, measurements in coherent structures, wind evolution, and methods for smoothly turning on and off the feed-forward controller so that it is operational only when LIDAR measurements are “accurate enough”.

12 References

1. Laks, J., Pao, L., Wright, A., Kelley, N., and Jonkman, B., "Blade pitch control with preview wind measurements," in Proc. 48th AIAA Aerospace Sciences Meeting, Orlando, FL, AIAA-2010-251, Jan. 2010.
2. Dunne, F., Pao, L., Wright, A., Jonkman, B., and Kelley, N., "Combining standard feedback controllers with feedforward blade pitch control for load mitigation in wind turbines," in Proc. 48th AIAA Aerospace Sciences Meeting, Orlando, FL, AIAA-2010-250, Jan. 2010.
3. Schlipf, D., and Kühn, M., "Prospects of a collective pitch control by means of predictive disturbance compensation assisted by wind speed measurements," in Proc. German Wind Energy Conference (DEWEK), Bremen, Germany, Nov. 2008.
4. Schlipf, D., Trabucchi, D., Bischoff, O., Hofsäß, M., Mann, J., Mikkelsen, T., Rettenmeier, A., Trujillo, J., and Kühn, M., "Testing of frozen turbulence hypothesis for wind turbine applications with a scanning LIDAR system," in Proc. International Symposium for the Advancement of Boundary Layer Remote Sensing, Paris, France, Jun. 2010.
5. Taylor, G., "The spectrum of turbulence," in Proceedings of the Royal Society of London, 1938.
6. Harris, M., Hand, M., and Wright, A., "LIDAR for turbine control," National Renewable Energy Laboratory, NREL/TP-500-39154, Golden, CO, Tech. Rep., Jan. 2006.
7. Laks, J., Pao, L., and Wright, A., "Combined feedforward/feedback control of wind turbines to reduce blade flap bending moments," in Proc. 47th AIAA Aerospace Sciences Meeting, Orlando, FL, AIAA-2009-687, Jan. 2009.
8. Mikkelsen, T., Hansen, K., Angelou, N., Sjöholm, M., Harris, M., Hadley, P., Scullion, R., Ellis, G., and Vives, G., "LIDAR wind speed measurements from a rotating spinner," in Proc. European Wind Energy Conference, Warsaw, Poland, Apr. 2010.
9. Jonkman, J., and Buhl, M., "FAST User's Guide," National Renewable Energy Laboratory, NREL/EL-500-38230, Golden, CO, Tech. Rep., 2005.
10. Jonkman, J., Butterfield, S., Musial, W., and Scott, G., "Definition of a 5-MW reference wind turbine for offshore system development," National Renewable Energy Laboratory, NREL/TP-500-38060, Golden, CO, Tech. Rep., 2009.
11. Kelley, N., and Jonkman, B., "Overview of the TurbSim stochastic inflow turbulence simulator," National Renewable Energy Laboratory, NREL/TP-500-39796, Golden, CO, Tech. Rep., 2007.
12. Jonkman, B., "TurbSim user's guide: Version 1.50," National Renewable Energy Laboratory, NREL/TP-500-46198, Golden, CO, Tech. Rep., 2009.

13. Frehlich, R., and Kavaya, M., "Coherent laser performance for general atmospheric refractive turbulence," *Applied Optics*, vol. 30, no. 36, pp. 5325–5352, Dec. 1991.
14. Frehlich, R., Meillier, Y., Jensen, M., Balsley, B., and Sharman, R., "Measurements of Boundary Layer Profiles in an Urban Environment," *Applied Meteorology and Climatology*, vol. 45, no. 6, pp. 821-837, June 2006.
15. Kelley, N., Osgood, R., Bialasiewicz, J., and Jakubowski, A., "Using wavelet analysis to assess turbulence/rotor interactions," *Wind Energy*, vol. 3, pp. 121–134, 2000.
16. Kelley, N., "The identification of inflow fluid dynamics parameters that can be used to scale fatigue loading spectra of wind turbine spectral components," National Renewable Energy Laboratory, NREL/TP-442-6008, Golden, CO, Tech. Rep., 1993.
17. Dunne, F., Pao, L., Wright, A., Jonkman, B., Kelley, N., and Simley, E., "Adding feedforward blade pitch control for load mitigation in wind turbines: Non-causal series expansion, preview control, and optimized FIR filter methods," in Proc. 49th AIAA Aerospace Sciences Meeting, Orlando, FL, Jan. 2011.
18. Laks, J, Pao, L., Simley, E., Wright, A., Kelley, N., and Jonkman, B., "Model predictive control using preview measurements from LIDAR," in Proc. 49th AIAA Aerospace Sciences Meeting, Orlando, FL, Jan. 2011.
19. Bossanyi, E. A., "Individual Blade Pitch Control for Load Reduction," *Wind Energy*, vol. 6, pp. 119–128, 2003.
20. Stol, K. and Fingersh, L., "Wind Turbine Field Testing of State-Space Control Designs," NREL/SR-500-35061, NREL Report, National Renewable Energy Laboratory, Golden, CO, 2004.
21. Wright, A., Fleming, P., and van Wingerden, J., "Refinements and Tests of an Advanced Controller to Mitigate Fatigue Loads in the Controls Advanced Research Turbine," Proc. 49th AIAA Aerospace Sciences Meeting, Orlando, FL, Jan. 2011.
22. Stol, K., Zhao, W., and Wright, A., "Individual Blade Pitch Control for the Controls Advanced Research Turbine (CART)," *ASME J. Solar Energy Engineering*, vol. 128, no. 4, pp. 498–505, Nov. 2006.
23. Bir, G., "Multi-blade Coordinate Transformation and its Application to Wind Turbine Analysis," Proceedings AIAA/ASME Wind Energy Symposium, Reno, NV, Jan. 2008.
24. Butterworth, J., Pao, L., and Abramovitch, D., "The Effect of Nonminimum-Phase Zero Locations on the Performance of Feedforward Model-Inverse Control Techniques in Discrete-Time Systems," Proc. American Control Conference, Seattle, WA, 2008, pp. 2696–2702.
25. Tomizuka, M., "Zero Phase Error Tracking Algorithm for Digital Control," *ASME J. Dyn. Sys., Meas. & Ctrl.*, vol. 109, pp. 65–68, Mar. 1987.

26. Wen, J. T. and Potsaid, B., "An Experimental Study of a High Performance Motion Control System," Proc. American Control Conference, June 2004, p. 5158–5163.
27. Potsaid, B., Wen, J. T., Unrath, M., Watt, D., and Alpay, M., "High Performance Motion Tracking Control for Electronic Manufacturing," ASME J. Dyn. Sys., Meas., & Ctrl, vol. 129, pp. 767–776, Nov. 2007.
28. Rigney, B. P., Pao, L. Y., and Lawrence, D. A., "Nonminimum Phase Dynamic Inversion for Settle Time Applications," IEEE Trans. Control Systems Technology, vol. 17, no. 5, pp. 989–1005, Sept. 2009.
29. Widrow, B. and Walach, E., Adaptive Inverse Control - a Signal Processing Approach, Wiley, Hoboken, NJ, 2008.
30. Matlab, Simulation and Model-Design Software Package, The MathWorks, Inc., Natick, MA.
31. Downing, S. D. and Socie, D. F., "Simple Rainflow Counting Algorithms," International J. Fatigue, vol. 4, no. 1, pp. 31–40, Jan. 1982.
32. Tomizuka, M. and Fung, D., "Design of Digital Feedforward/Preview Controllers for Processes with Predetermined Feedback Controllers," ASME J. Dyn. Sys., Meas. & Ctrl., vol. 102, pp. 218–225, Dec. 1980.
33. Simley, E., Pao, L. Y., Frehlich, R., Jonkman, B., and Kelley, N., "Analysis of Wind Speed Measurements using Coherent LIDAR for Wind Preview Control," Proc. AIAA Aerospace Sciences Meeting, Orlando, FL, Jan. 2011.
34. Goldberg, D. E., Genetic Algorithms in Search Optimization and Machine Learning, Addison Wesley, 1989.
35. Devasia, S., Paden, B., and Chen, D., "Nonlinear Inversion-Based Regulation," IEEE Transactions on Automatic Control, vol. 41, no. 7, pp. 930–942, Jul. 1996.

Appendix: Derivation of Measurement Error Sensitivity to Measurement Angle

Without loss of generality, consider a LIDAR measurement of wind velocity where the LIDAR is located at the origin [see Figure 2 (a)] and the measurement point is contained in the xz plane with $y = 0$, upwind from the LIDAR. Consider the wind to have a positive u component, aligned with the x direction, which will be referred to as U . The wind velocity vector has a transverse component in the yz plane with magnitude $\alpha = \sqrt{v^2 + w^2}$ and uniformly distributed random angle, ψ , in the yz plane. If the LIDAR measures this wind velocity with a measurement angle θ , the detected radial velocity is given by

$$u_r = \cos \theta \cdot U + \sin \theta \sin \psi \cdot \alpha. \quad (0.1)$$

The estimate of the u component, using Eq. (2.9), is given by

$$\hat{u} = \frac{u_r}{\cos \theta} = U + \tan \theta \sin \psi \cdot \alpha \quad (0.2)$$

and therefore the measurement error, $\hat{u} - U$, is

$$\text{err}(\hat{u}) = \tan \theta \sin \psi \cdot \alpha. \quad (0.3)$$

When many wind speed measurements are made, the RMS measurement error is calculated as

$$\sigma_{\text{err}} = \sqrt{\tan^2 \theta \sin^2 \psi \cdot \alpha^2}. \quad (0.4)$$

Since θ is constant and ψ and α are independent random variables, Eq. (0.4) becomes

$$\sigma_{\text{err}} = \tan \theta \sqrt{\sin^2 \psi} \sqrt{\alpha^2}. \quad (0.5)$$

Finally, since the RMS value of $\sin^2 \psi$ is $\frac{\sqrt{2}}{2}$, the RMS measurement error is given by

$$\sigma_{\text{err}} = \frac{\tan \theta \cdot \alpha_{\text{RMS}}}{\sqrt{2}} \quad (0.6)$$

where α_{RMS} is the RMS magnitude of the transverse wind component.